Volume 52
DOE/DP40200-229

LLE Review

Quarterly Report

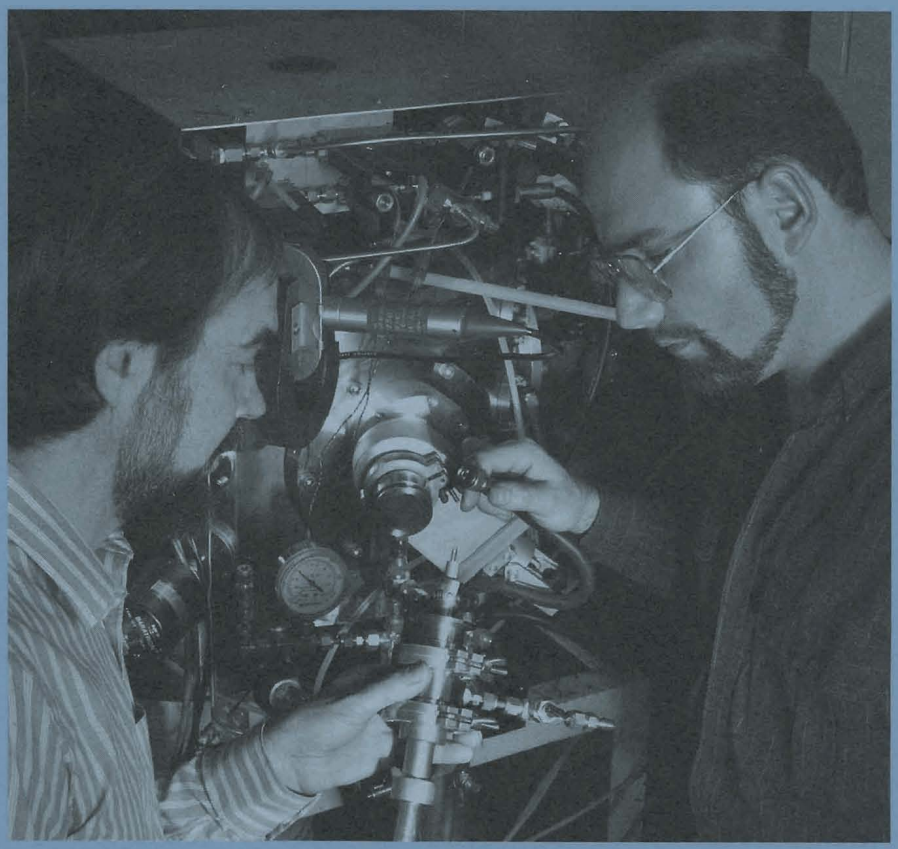

July–September 1992

Laboratory for Laser Energetics
College of Engineering and Applied Science
University of Rochester
250 East River Road
Rochester, New York 14623-1299

Volume 52
DOE/DP40200-229

LLE Review

Quarterly Report

Editor: R. W. Short
(716) 275-4075

July–September 1992

Laboratory for Laser Energetics
College of Engineering and Applied Science
University of Rochester
250 East River Road
Rochester, New York 14623-1299

IN BRIEF

This volume of the LLE Review, covering the period July–September 1992, contains articles on methods of balancing the beam power on the OMEGA Upgrade and on the damping of ion-sound waves in laser-produced plasmas. The advanced technology section includes reports on optical nonlinearities in high-temperature superconductors, a method of increasing gas retention time for laser-fusion targets, and a study of stimulated Raman scattering of laser beams in air.

Highlights of the research reported in this issue are

- An efficient method has been developed for balancing the power in the 60 beams of the OMEGA Upgrade. The method can achieve 2% power balance for both main and foot beams using only four system shots.

- A study of ion-sound-wave damping has substantially revised and expanded our knowledge of this effect. The damping of ion waves can have important consequences for laser-plasma interaction.

- The use of femtosecond laser pulses to study the properties of thin-film, high-temperature superconductors is discussed.

- A method for increasing the gas retention time of polymer-shell laser-fusion targets by overcoating them with a thin layer of aluminum is described.

- A code has been developed to study stimulated rotational Raman scattering in high-power laser beams propagating through air.

CONTENTS

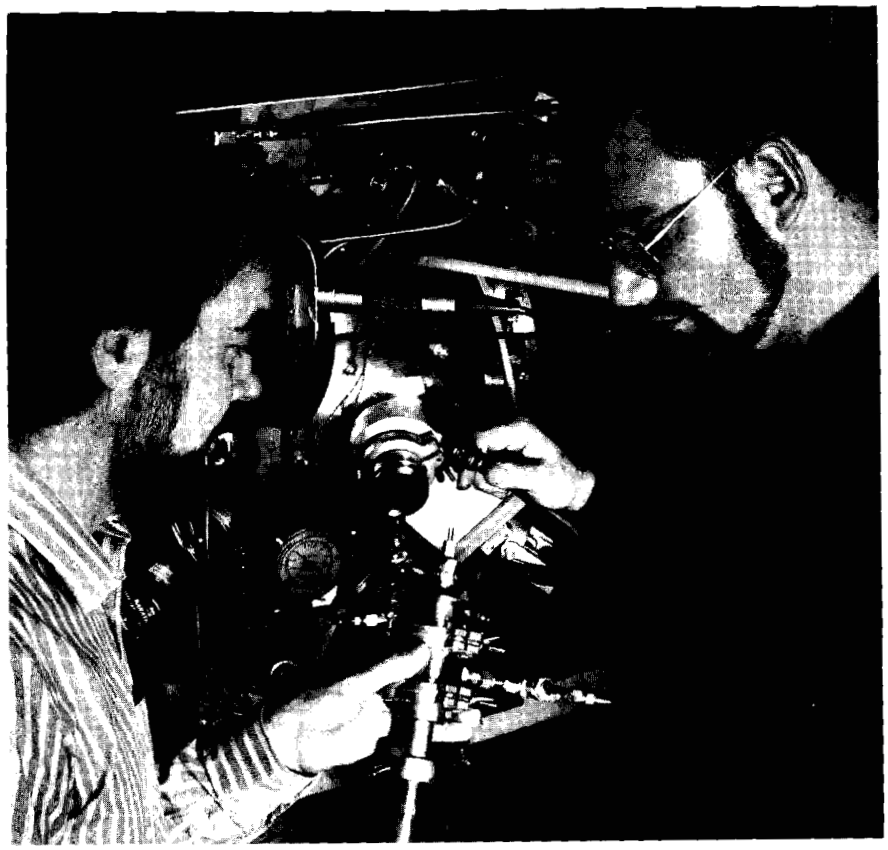

Roger Gram, Research Engineer, and Mark Wittman, Senior Technical Associate, prepare polymer-shell targets for sputter-coating with aluminum. A thin aluminum layer significantly increases the retention time for gases, while remaining sufficiently transparent to allow interferometric measurement of gas content. These shells would otherwise be much too permeable to retain gases long enough to conduct ICF experiments.

Section 1
PROGRESS IN LASER FUSION

1.A A Strategy for Laser-Beam Power Balance on the OMEGA Upgrade

One of the requirements for the OMEGA Upgrade laser system[1] is that it deliver its energy to the target with an irradiation perturbation caused by power imbalance of 1% or better.[2] This requirement is based on results from two-dimensional computer simulations in which OMEGA Upgrade high-gain targets were driven by a spatially perturbed laser-irradiation distribution resulting from beam power imbalance. Such a distribution, which consists mainly of low-order Legendre modes (<20), produces an implosion asymmetry that grows secularly and has the potential for reducing the target performance by mixing pusher and core material.[3] It is, therefore, necessary to control the irradiation power balance throughout most of the laser pulse.

The OMEGA Upgrade consists of 60 beams produced by three sets of beam splitters, A, B, and D, as shown schematically in Fig. 52.1. (The D splitter is actually composed of two different splitters separated by a spatial filter. This is treated as a single splitter in the power-balance analysis.) A set of splitters and the associated optics and amplifier(s) are defined as a splitter group. The laser pulse, shown in Fig. 52.2, is comprised of a slow-rising, low-power foot pulse and a fast-rising, high-power main pulse. The two pulses are coaxially propagated through the laser system, with the foot pulse in the center and the main pulse on the outside. Since several beams overlap on target, the 1%-rms power-balance requirement over the target surface is equivalent to a 3%–5% beam-to-beam requirement at the output of the laser beams. This power-balance level is needed throughout the last half of the foot pulse and through the early part of the main pulse.[3]

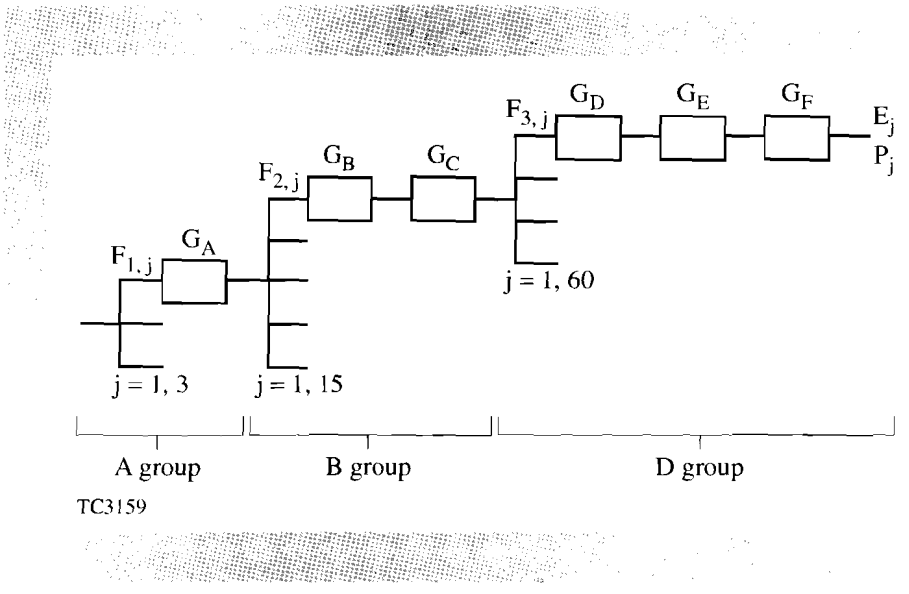

Fig. 52.1
Schematic of the OMEGA Upgrade laser system and notation used in the analysis of the power-balance model.

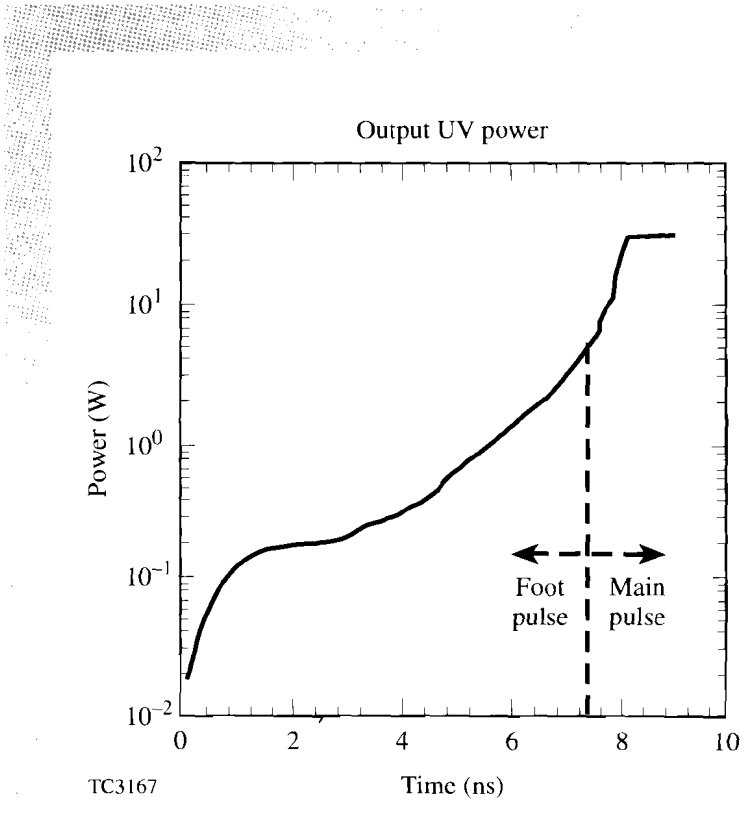

Fig. 52.2
Typical temporal UV pulse shape for high-gain target experiments. The pulse is divided into a low-intensity foot pulse and a high-intensity main pulse. The two pulses are propagated coaxially, with the foot pulse inside the main pulse.

In this article we present a strategy to obtain power balance on the OMEGA Upgrade in which the output energy and the peak power are measured and the D-splitter fractions and the F-amplifier gain (G_F in Fig. 52.1) are adjusted. Only the contributions to power imbalance caused by beam-splitter setting variations, variations of the amplifier voltages, and inaccurate knowledge of the losses in the beamline are considered. Other contributors to power imbalance, such as variations in beam areas (that affect the frequency-conversion efficiency), conversion crystal settings, and beam timing, are not considered.

This article is divided into four sections. (1) Conditions of the strategy and the equations relating the output energy and power in terms of split fractions and amplifier gains are presented; (2) the laser propagation model is described and the dependence of the output energy and peak power on the split fractions and amplifier gains is presented; (3) a description of the method and a presentation of the results follows; and finally (4) we present a discussion of limitations and our conclusion.

General Principles

Any method for obtaining the desired power balance would be subject to the following practical constraints: First, tuning of the energy and power balance must be done only on the basis of known and controllable variations in the split fractions and amplifier gains because initial settings are not accurately known. Second, the only place where beam measurements can be accurately made is at the output of the last amplifier (IR measurement) or at the output of the frequency-conversion crystals (UV measurement). No accurate measurements can be carried out at the beam splitters or after any amplifier because there is not enough space between the laser components for deploying the instruments. Third, the only two beam-to-beam quantities that can be measured with a relative accuracy of a few percent are the total energy and the peak power. Finally, the power-balance tuning must be carried out with the least number of full-power shots (five or less) and with the smallest amount of component manipulation (varying split fractions or amplifier voltages).

Power balance in the case of the OMEGA Upgrade laser is complex because the 60 final beams are coupled through the three sets of splitters. Therefore, the input to each chain cannot be independently controlled. Another constraint on the control of the input energy is that the sum of the split fractions must evidently be equal to or less than unity. It is possible for the sum of the split fractions to be less than unity because the reflectivity of the individual mirror is controlled by its angle with respect to the beam. In such a case, laser energy is discarded. The most general form of a transfer equation for the output energy E_j and peak power P_j of the j^{th} output beam in terms of the split fractions $F_{i,j}$ and the small-signal gain $G_{i,j}$ in the last amplifier in each splitter group (amplifiers A, C, and F, respectively) is given by

$$\Delta E_j = \sum_{i=1}^{3} \left\{ \left(\frac{\partial E_j}{\partial F_{i,j}} \right)_{G_{i,j}} \Delta F_{i,j} + \left(\frac{\partial E_j}{\partial G_{i,j}} \right)_{F_{i,j}} \Delta G_{i,j} \right\}$$

$$\Delta P_j = \sum_{i=1}^{3} \left\{ \left(\frac{\partial P_j}{\partial F_{i,j}} \right)_{G_{i,j}} \Delta F_{i,j} + \left(\frac{\partial P_j}{\partial G_{i,j}} \right)_{F_{i,j}} \Delta G_{i,j} \right\} , \quad (1)$$

where ΔE_j is the variation in the output energy of the j^{th} beam, ΔP_j is the variation in the peak power of the j^{th} beam, $F_{i,j}$ is the split fraction of the i^{th} splitter (A, B, and D) and the j^{th} beam of the splitter, and $G_{i,j}$ is the small-signal gain of the last amplifier in the j^{th} beam of the i^{th} splitter group. The index i is over the three splitters in the most general case. Although the functional dependence of the output energy and peak power with split fraction and F-amplifier gain is far from linear over the entire range of the dependent variables (see the following), we assume that it is linear over the range through which the quantities will be varied during the power-balance tuning:

$$\Delta E_j = \sum_{i=1}^{3} \left[a_{i,j} \Delta F_{i,j} + b_{i,j} \Delta G_{i,j} \right]$$

$$\Delta P_j = \sum_{i=1}^{3} \left[c_{i,j} \Delta F_{i,j} + d_{i,j} \Delta G_{i,j} \right] , \quad (2)$$

where the constants $a_{i,j}$, $b_{i,j}$, $c_{i,j}$, and $d_{i,j}$ can be obtained by varying each split fraction $F_{i,j}$ and each amplifier gain $G_{i,j}$ while keeping the other components constant, and measuring the change in the output energy and peak power. To this set of equations must be added the requirement that the sum of the split fractions (k) in a given splitter cluster (i) be unity:

$$\sum_{k} F_{i,k} = 1 . \quad (3)$$

The upper limit of the sum depends on the splitter: it is 3 for the single A splitter, 5 for each of the five B splitters, and 4 for each of the 15 D splitters.

There are several methods by which the power balance could be obtained. The most general way is to solve the entire set of 139 linear equations, 120 given by Eq. (2) and 19 from Eq. (3) for each splitter. The independent variables are the 78 split fractions (see Fig. 52.1: 3 + 15 + 60) and the small-signal gains from the 60 F-amplifers for a total of 138. The missing variable could be the average output energy (see the following). The dependent variables are the 60 laser-output-energy values and the 60 peak-power values. Another method is to balance each split cluster starting with the D-splitter groups. First, both the energy and the peak power are balanced for each of the four beams in each of the D-splitter groups by varying the splitter fractions and the F-amplifier gain. This leaves 15 unbalanced beams in the B-splitter group. Each of these 15 beams is then balanced by using the output energy and the peak power summed over each of the D-splitter groups. The three unbalanced beams in the A-splitter group are then balanced by using the output energy and the peak power summed over the

three groups of 15 beams. A third method is an iterative scheme in which the laser beams are first balanced for output energy by varying the split fractions and then balanced for peak output power by varying the F-amplifier small-signal gain. In all the methods, measurements need to be carried out with full-power shots since the large-signal gain differs significantly from the small-signal gain because of saturation effects.

Modeling and Results

To simulate the various possible schemes, beam propagation through the OMEGA Upgrade laser is modeled with a one-dimensional code in which the foot pulse and the main pulse are propagated separately. Both the laser beam and the amplifiers are divided into small slices in time and space, respectively. From the given initial amplifier gain $G_0 = \exp(\alpha_0 L)$, where α_0 is the initial gain coefficient and L the amplifier length, the initial gain per amplifier slice is calculated as $\Delta G_0 = \exp[\ln(G_0)/N]$, where N is the number of amplifier slices. The first step in the transport of the beam through an amplifier is to modify the input fluence by the energy split fraction, any beam expansion, and the losses associated with that amplifier. When the beam is transported through the E and F amplifiers, the input fluence is reduced by a factor of 1.5 because the disks are tilted at a 45° angle. The slices of the beam are then transported through the amplifier and their fluence is calculated according to $F_{out}(x, t) = F_{in}(x, t) \exp[\Delta G(x, t)]$. Gain depletion in an amplifier slice is taken into account by decreasing the stored energy in the slice by the amount given to the beam. At the end of the chain, frequency conversion is calculated from a third-order polynomial fit to the conversion efficiency as a function of the laser intensity. Unless otherwise noted, the output energy and the peak power are "measured" after the conversion crystal from the UV output. The propagation code can also be run in the "oscillator-pulse" mode by reducing the amplifier gains to a very small value. The laser parameters used in the simulation are given in Table 52.I.

The first step in the modeling is to calculate the input laser beam that will produce the desired beam shape shown in Fig. 52.2. This is done by propagating the pulse in Fig. 52.2 backward through a single chain with nominal component settings. The resulting foot and main pulses are displayed in Fig. 52.3. The foot pulse is a fast-rising pulse that is monotonically increasing until it is cut off at the start of the main pulse. The main pulse starts at a lower value than the end of the foot pulse because the gain for the first photon is larger than the large-signal gain that controls the end of both pulses. The junction of the two pulses will not be addressed here.

The dependence of the output energy per beam on the split fraction of the A, B, and D splitters and on the amplifier gain of the A, C, and F amplifiers is shown in Fig. 52.4. Similarly, the dependence of the peak power on the split fractions and amplifier gains is shown in Fig. 52.5. The dashed curves and lines are the nominal operating conditions, which are the perfect split fraction and the nominal gain of the amplifiers as listed in Table 52.I. For ease of comparison the curves are plotted over the same range of axis values and the gains are varied over a 50% range. The effects of gain depletion and saturation are evident from the leveling of the output energy and from the ultimate decrease of the peak power

Table 52.I: Parameters of the OMEGA Upgrade laser. Two splitters between the C and the D amplifiers were treated as a single four-way splitter. The performance numbers were obtained with more detailed propagation code than the one used in this article.

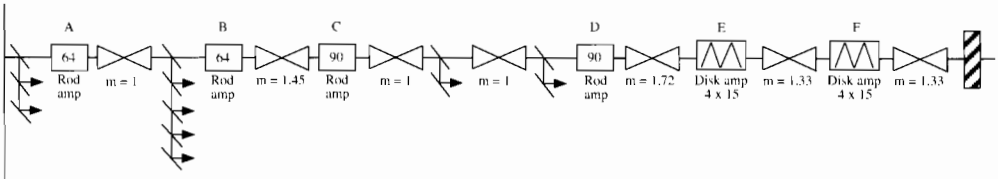

																	3ω
Transmission	0.31	0.88	0.99	0.17	0.88	0.99	0.85	0.99	0.47	0.99	0.47	0.88	0.96	0.96	0.99	0.95	0.99	0.97
Main pulse																		
First photon gain			16.0		16.0		9.0					9.0		4.2		3.0		
Energy (J)	0.45	5.2	5.2	1.0	11.0	11.0	69	68	34	33	16	94	93	320	310	740	730	615
Avg. fluence (J/cm^2)	.065	0.61	0.61	0.11	1.0	0.47	2.3	2.3	1.1	1.1	0.52	2.5	0.83	2.8	1.55	3.65	1.8	1.6
Foot pulse																		
First photon gain			9.6		9.6		6.4					6.4		4.2		3.0		
Energy (J)	0.54	4.0	4.0	0.75	5.4	5.3	22	22	11	10	5.1	21.5	21	70	69	160	160	82
Avg. fluence (J/cm^2)	0.81	1.3	1.3	0.24	1.7	0.79	3.2	3.2	1.6	1.5	0.72	2.9	1.1	3.4	1.9	4.3	2.1	1.2

TC3146

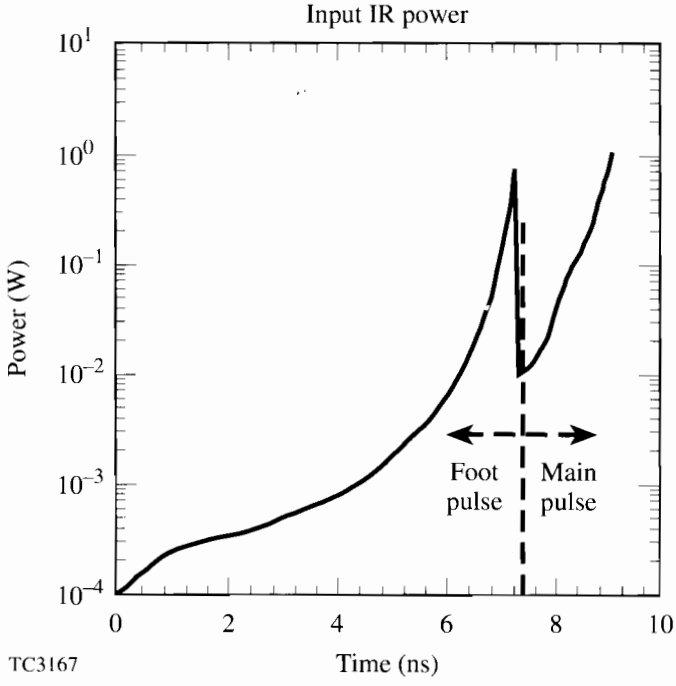

Fig. 52.3
Input IR pulse shape of the laser chain obtained by propagating the pulse in Fig. 52.2 backward. The jump at the junction of the two pulses occurs because the small-signal gain at the foot of each pulse is larger than the large-signal gain at the end of each pulse.

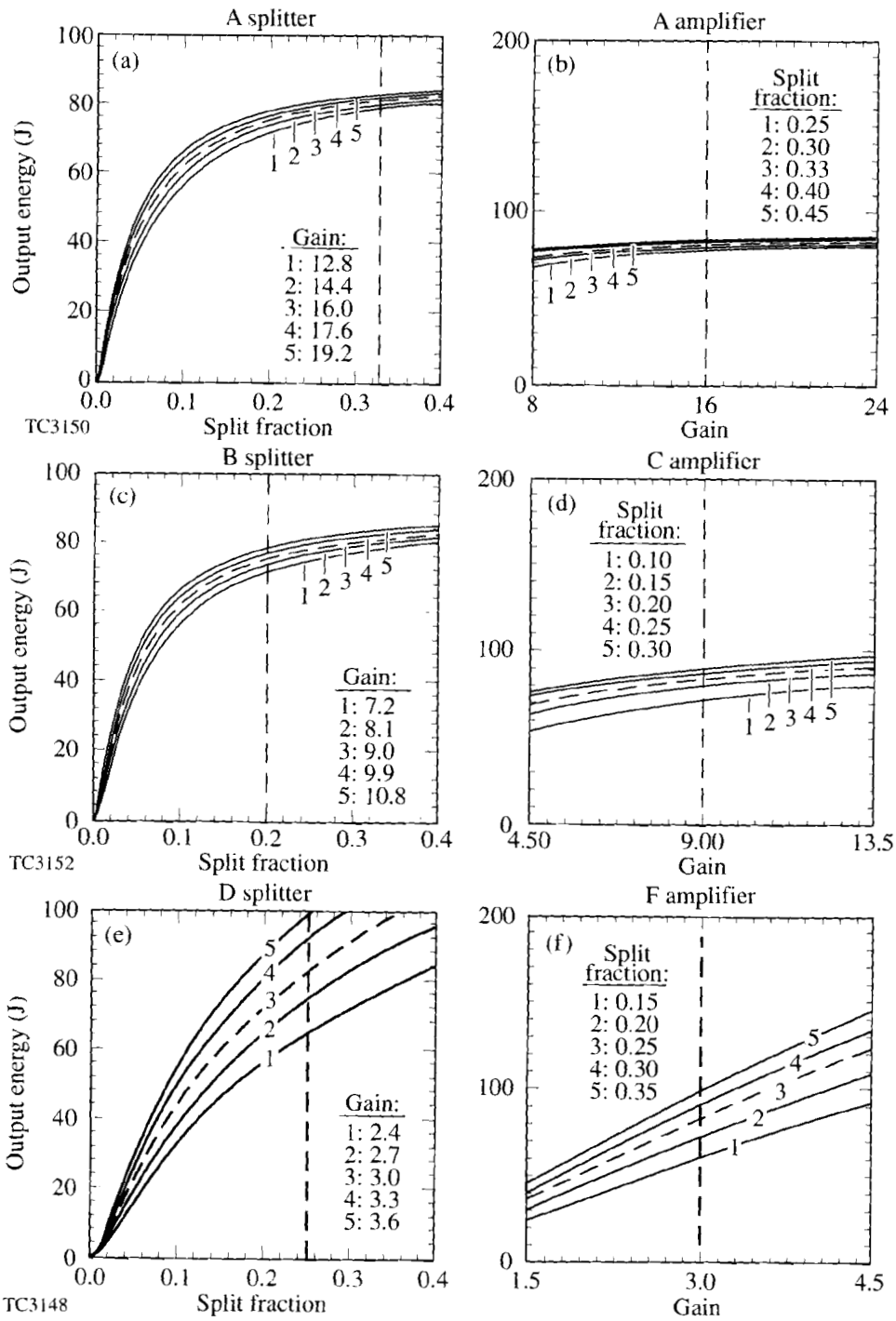

Fig. 52.4
Dependence of the output UV energy for the foot pulse on the amplifier gains and the split fractions. (a) A splitter and (b) A amplifier; (c) B splitter and (d) C amplifier; (e) D splitter and (f) F amplifier.

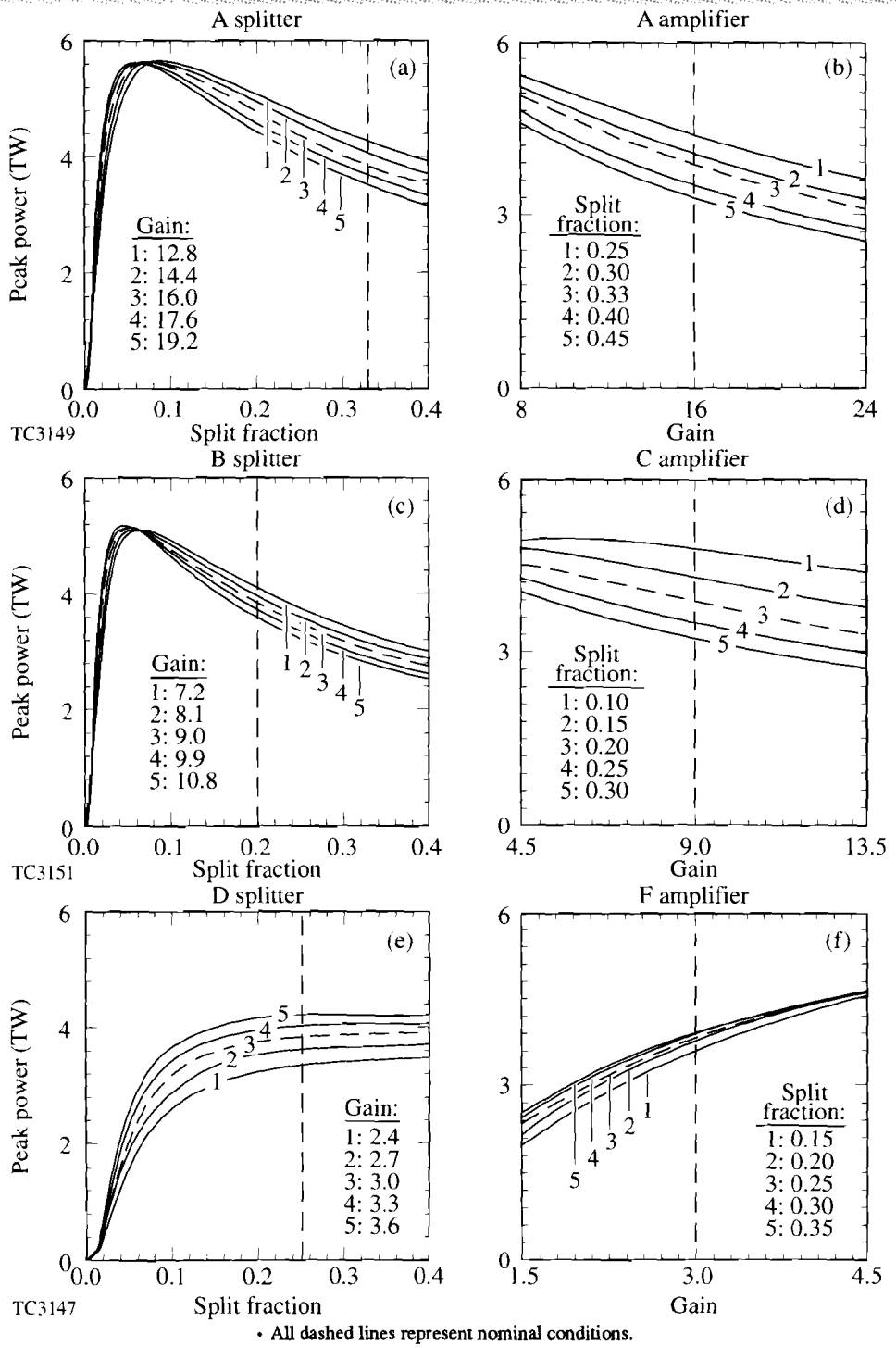

Fig. 52.5
Dependence of the peak UV power for the foot pulse on the amplifier gains and the split fractions. (a) A splitter and (b) A amplifier; (c) B splitter and (d) C amplifier; (e) D splitter and (f) F amplifier.

when split fractions and amplifier gains are increased. In particular, for the case of the D splitter [Fig. 52.5(e)], the peak power is practically independent of the split fraction near the operating condition and thus can only be controlled by varying the amplifier gain. The important point to note in these figures is the lessening of the "leverage" available to vary the output energy and peak power as one moves from the D-splitter group to the A-splitter group, i.e., the slope of the curves becomes flatter. This is especially evident when the dependence of the output energy on the amplifier gains is compared for each amplifier: for the A and C amplifiers [Figs. 52.4(b) and 52.4(d)] the output energy is almost independent of the gain, which means that the gain of these two amplifiers cannot be used to correct any output-energy imbalance between clusters of four beams for the D amplifier and clusters of 15 beams for the A amplifier. On the other hand, this low sensitivity increases the tolerance for the precise tuning of the amplifier gains in the first three stages of the laser. Finally, Figs. 52.4 and 52.5 show that the dependence of the output energy and peak power on the split fractions and amplifer gains is nearly linear in most cases near the operating points so that the linear relationships in Eq. (2) can be used in the analysis.

This lack of leverage means that any method that includes tuning the components in the A and B groups cannot improve much on results obtained with only the D group. In the method by which the individual clusters in the D group are first balanced, followed by balancing the B and A clusters, no values of the splitter fractions and amplifier gains in the A group could be found to reduce the power imbalance to the desired values. The method by which the entire system of 139 equations is solved does provide a solution, but the method tends to favor energy balance rather than peak-power balance. This probably results from the inability to tune the splitters and the amplifier gains in the A and B groups to provide both energy and peak-power balance. Finally, iterative methods, such as first balancing the energy and then the peak power, were found to require too many iterations; hence, too many full-power shots to converge.

The method proposed in this article balances the beam power by varying the split fractions in the 15 D splitters and the gain of the 60 F amplifiers. The measured quantities are the output energy and the peak power for each beam. This scheme works because the splitter fraction controls the power early in the pulse, while the amplifier gain controls the power late in the pulse. Not all the constants in Eq. (2) need to be obtained. Model results indicate that the value of these constants does not differ appreciably from beam to beam and that power balance is obtained as efficiently with four constants as with the entire set. Eq. (2) thus reduces to

$$\Delta E_j = a_1 \Delta F_j + a_2 \Delta G_j$$

$$\Delta P_j = b_1 \Delta F_j + b_2 \Delta G_j \quad , \tag{4}$$

where ΔF_j is now the D-splitter fraction and ΔG_j is the F-amplifier gain for beam j. Only two beams (in one cluster) need to be fired to obtain the four constants in Eq. (4). With one beam, a_1 and b_1 are obtained by varying one of the D-splitter fractions, keeping the gain constant, and measuring the total energy and the peak

power. With the second beam, a_2 and b_2 are obtained by varying the F-amplifier gain, keeping the splitter fraction constant, and measuring the same quantities. A full-power shot with all beams is still required to obtain baseline measurements of the output energy and peak power in order to balance all the beams.

The beams are balanced by finding the values of ΔF_j and ΔG_j in Eq. (4) that are needed to modify the beam outputs by the quantities ΔE_j and ΔP_j, which are the differences between the beam output and a desired average value. For each cluster of four beams, this is obtained by solving the set of linear algebraic equations

$$
\begin{aligned}
a_1 \Delta F_1 + a_2 \Delta G_1 &= E_{\text{av}} - E_1 \\
a_1 \Delta F_2 + a_2 \Delta G_2 &= E_{\text{av}} - E_2 \\
a_1 \Delta F_3 + a_2 \Delta G_3 &= E_{\text{av}} - E_3 \\
a_1 \Delta F_4 + a_2 \Delta G_4 &= E_{\text{av}} - E_4 \\
\\
b_1 \Delta F_1 + b_2 \Delta G_1 &= P_{\text{av}} - P_1 \\
b_1 \Delta F_2 + b_2 \Delta G_2 &= P_{\text{av}} - P_2 \\
b_1 \Delta F_3 + b_2 \Delta G_3 &= P_{\text{av}} - P_3 \\
b_1 \Delta F_4 + b_2 \Delta G_4 &= P_{\text{av}} - P_4 \\
\\
\Delta F_1 + \Delta F_2 + \Delta F_3 + \Delta F_4 &= 0 \ , \qquad (5)
\end{aligned}
$$

where E_{av} and P_{av} are the desired average output energy and peak power per beam and E_j and P_j ($j = 1, 4$) are the output energy and peak power for each beam. The last expression is another way to state the requirement that the sum of the split fractions be unity, assuming that it was initially unity. For the 15 clusters we now have 135 equations (60 for the energy balance, 60 for the power balance, and 15 for the split-fraction sums), and 122 unknowns (120 unknown values of ΔF and ΔG, and the two unknown quantities E_{av} and P_{av}). Thus the system of equations is overspecified. If each cluster were to be solved separately, obtaining different values of E_{av} and P_{av} for each cluster, then we would have 15 well-specified systems of equations per cluster. Energy and peak-power imbalance, however, would remain between the clusters. Attempts to balance these clusters by tuning the A and B splitters and the A and C amplifiers have been unsuccessful because of the lack of "leverage" of the components.

In the method chosen, the last equation is dropped, E_{av} and P_{av} are computed from the beam energies, and peak powers are measured in full-power shots. Since the condition on the sum of the split fractions is relaxed, that sum can now exceed unity. When this occurs, it means that there are no solutions to the system of equations that would result in zero variation in the output power and peak power, while keeping the sum to unity in all the clusters. To maintain the sum of the split fractions as close to unity as possible, so as to keep the loss of laser energy to a minimum, the split fractions are corrected in the following manner.

The largest value from the 15 sums of split fractions (in the 15 D-splitter clusters) is found and all the split fractions are divided by that value. Thus, the sum of the fractions for a single cluster is unity and the sums for the other clusters are slightly less than unity, resulting in a slight loss in laser output energy.

The solution requires several iterations because of the slight nonlinearity in the dependence of the output energy and peak power on the splitter fraction and F-amplifier gain (see Figs. 52.4 and 52.5). Steps for balancing the beams are as follows:

1. An initial full-power shot is taken at nominal conditions. This shot can be the full-power shot required to obtain the constants in Eq. (4).

2. The average energy E_{av} and average peak power P_{av} are computed from the measured energy and peak power of the 60 beams.

3. The following set of 120 equations is solved for ΔF_i and ΔG_i using a conventional method such as Gaussian elimination:

$$a_1 \Delta F_i + a_2 \Delta G_i = E_{av} - E_i$$

$$b_1 \Delta F_i + b_2 \Delta G_i = P_{av} - P_i \qquad i = 1,60.$$

4. The split fractions are corrected so that the largest sum of the split fraction is unity.

5. The D-splitter fractions and F-amplifier gains are modified by ΔF_i and ΔG_i, respectively, and a full-power shot is taken to check the power balance. At this point an updated value of E_{av} is obtained if needed for the next iteration. (Updating P_{av} results in slightly larger energy and peak-power imbalance for a given iteration step.)

6. If necessary, another iteration is carried out by returning to step 3.

One full-power shot is required per iteration, after the initial full-power shot at nominal conditions and a full-power shot with only four output beams to obtain the constants. For the purpose of this article, a final shot with both the foot pulse and the main pulse was simulated to obtain the rms variations of the output energy, the power at the front of each pulse, and the peak power.

The model was run for a case where all the split fractions, the amplifier gains, and the stage losses were initialized with variations obtained from a series of Gaussian random numbers with $\sigma_{rms} = 0.02$ to simulate the accuracy with which these components can be initially set. Table 52.II shows a sample of the variation percentage of the components in one beamline. The set of variations can be considered to be somewhat pessimistic since several variations exceed 2%. Tight controls during the construction of the laser would probably eliminate any variations above 2%. The initial foot-pulse and main-pulse energies were 82.2 J and 781 J, respectively. A 1% error (also from a Gaussian random-number distribution) was applied to the measurements of the output energy and peak power. A 2% error in the measurements makes it impossible to balance the

Table 52.II: Sample of the applied percent σ_{rms} variations obtained from a Gaussian random-number distribution with $\sigma_{rms} = 0.02$.

A group			B group					D group						
$\frac{\Delta F_s}{F_s}$	$\frac{\Delta L}{L}$	$\frac{\Delta G}{G}$	$\frac{\Delta F_s}{F_s}$	$\frac{\Delta L}{L}$	$\frac{\Delta G}{G}$	$\frac{\Delta L}{L}$	$\frac{\Delta G}{G}$	$\frac{\Delta F_s}{F_s}$	$\frac{\Delta L}{L}$	$\frac{\Delta G}{G}$	$\frac{\Delta L}{L}$	$\frac{\Delta G}{G}$	$\frac{\Delta L}{L}$	$\frac{\Delta G}{G}$
1.8	–0.59	–3.1	–0.06	–0.37	0.62	0.60	2.9	–1.3	2.6	1.9	0.72	–2.8	–1.5	4.8

TC3130

beams. Figure 52.6 shows the asymptotic improvement in the fractional standard deviation (standard deviation divided by the mean) of the output energy (a), the front power (b), and the peak power (c) with the number of iterations for the foot pulse. The standard deviation for the peak power and the energy drops rapidly after five iterations below 10^{-3}, while the standard deviation for the front power does not drop below 0.02 and does not improve beyond the third iteration. The temporal dependence of the fractional standard deviation of the power, at nominal conditions and after three iterations, for both the foot pulse and the main pulse is shown in Fig. 52.7. The deviation is the largest early in the pulse because the gain at that time (the small-signal gain) is larger than the large-signal gain at the end of the pulse. The jump in the deviation at the junction of the foot and main pulses is also caused by the same effect. The deviation at the front of the pulse is the same for both the foot pulse and the main pulse. This is important because the power balance must be as good early in the main pulse as it is during the foot pulse. The final foot-pulse and main-pulse energies are 77 J and 730 J, respectively—a reduction of about 6% for both pulses.

Restrictions on the value of gain of the F amplifier have not yet been considered. The design of that amplifier actually restricts the "head room," or the amount by which the gain can be increased over the nominal gain, to 5% of the nominal gain. In the previous example, the gains of 24 of the 60 amplifiers were larger than 5% nominal, with some gains as high as 30% higher than nominal. Four entire clusters had gains that exceeded the design head room. This problem can be partially remedied by inspecting the beams or clusters that require the large gains and fixing or swapping the components that cause the demand for large gains. Derating the laser energy would, of course, also solve the problem.

The fact that a beam or a cluster requires a larger gain than the others is not necessarily because the input to that beam or the cluster is lower than that of the others. The large gain requirement is caused by the "competition" between the splitter fractions and the amplifier gains. For demonstration purposes, we consider "balancing" a single beam, i.e., computing how much the split fraction ΔF and the amplifier gain ΔG need to be changed so as to remove a given energy and peak-power variation, ΔE and ΔP, respectively. The solution of Eq. (4) for ΔG in the case of a single beam is given by

$$\Delta G = \frac{-a_2 \Delta E + a_1 \Delta P}{a_1 b_2 - a_2 b_1}$$

For a given ΔE and ΔP, ΔG can be either positive or negative. As an example, we consider beam 1 in the solution discussed previously. The constants are $a_1 = 203\ \text{J}^{-1}$, $a_2 = 29\ \text{J}^{-1}$, $b_1 = 1.15\ \text{TW}^{-1}$, and $b_2 = 0.71\ \text{TW}^{-1}$. The energy and peak-power variations from the mean values are $\Delta E = -8.0$ J and $\Delta P = -0.02$ TW. The solution to the system of equations

$$\begin{aligned} 203\ \Delta F + 29\ \Delta G &= -8.0 \\ 1.15\ \Delta F + 0.71\ \Delta G &= -0.02 \end{aligned}$$

is $\Delta F = -0.046$ and $\Delta G = 0.043$. Thus, while balancing the energy requires decreasing the output of beam 1 by 8 J, this is actually done by decreasing the split fraction and *increasing* the amplifier gain. The beam can only be balanced by subtracting large changes in the energy caused by changes in the split fraction and the gain (hence, the term "competing" used previously). The problem arises from balancing the output energy and peak power in the beams simultaneously. Changes in output energy (or in peak power) cannot be "shared" by the two components because a change in ΔF and ΔG that satisfies the needed change in ΔE cannot provide the change that would balance the peak power.

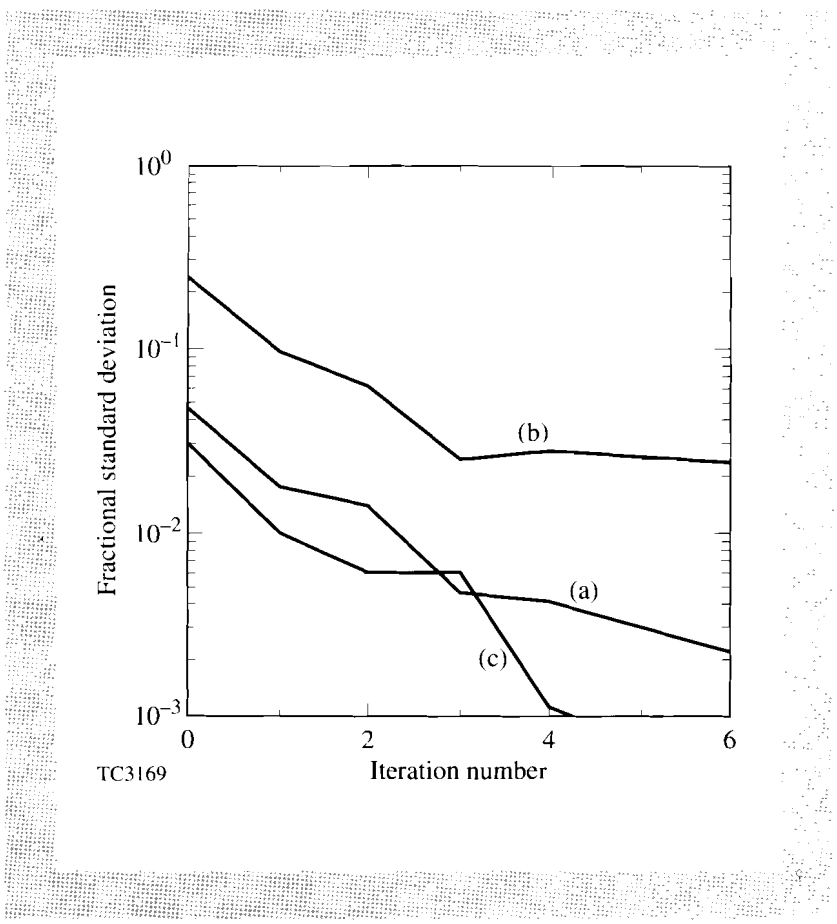

Fig. 52.6
Dependence of the fractional standard deviation on the number of iterations for (a) the output energy; (b) the power at the front of the pulse; (c) the peak power.

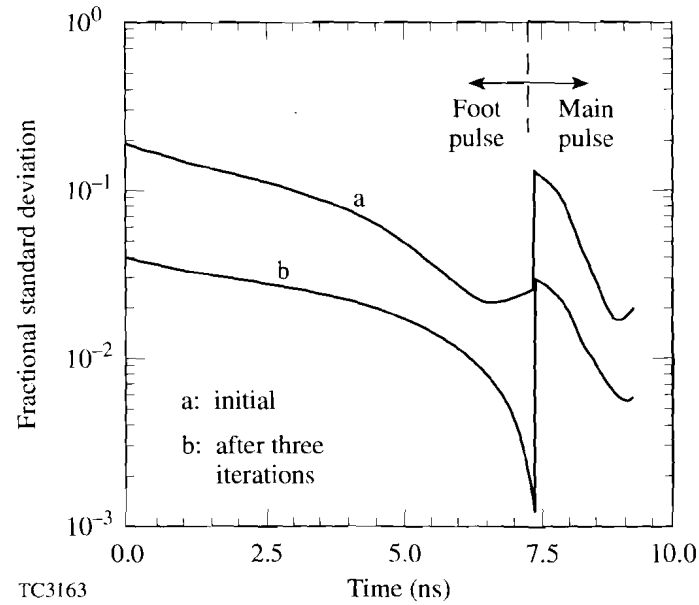

Fig. 52.7
Temporal dependence of the fractional standard deviation for the entire pulse for nominal conditions and after three iterations.

A final topic of interest is the use of a Gaussian pulse, which is easy to produce, to tune the splitter fractions and the F-amplifier gains. Again the tuning is done over a few iterations. Figure 52.8(a) shows the nominal temporal-fractional deviation and the deviation after three iterations for a 1.8-ns Gaussian pulse. The energy balance is about 1%, and the power balance is worse past the peak of the pulse than in the early part of the pulse. The foot pulse in Fig. 52.3 is then propagated through the chain with the splitter fractions and the amplifier gains obtained by tuning the Gaussian pulse. The resulting fractional deviations are plotted in Fig. 52.8(b) as a function of time for the nominal case and after three iterations in the tuning of the Gaussian pulse. The energy balance is now 1.2%, the power balance at the front is 6.6%, and at the peak power is 0.8%. Thus, when a Gaussian pulse is used to tune the splitter fractions and the amplifier gains, the resulting energy and power balance are about a factor of 2 to 3 worse than if the tuning was done with the actual foot pulse in Fig. 52.3.

Conclusions

We have proposed a strategy for balancing the power in the OMEGA Upgrade laser that satisfies the following basic requirements: The power balance at the laser output must be better than 5%; beam measurements can only be done at the laser output; the least number of components should be tuned; and the number of full-power shots should be five or fewer. Also, it was assumed that the split fractions, the amplifier gains, and the losses were known to within a 2% Gaussian random error and that the measurements could be carried out with a 1% error. The method proposed involves measuring the output energy and the peak power, and tuning the D-splitter fractions and the F-amplifer gains. The tuning, which can be carried out with a minimum of three full-power, 60-beam shots and one full-power, two-beam shot, provides a power balance better than 2% over the entire

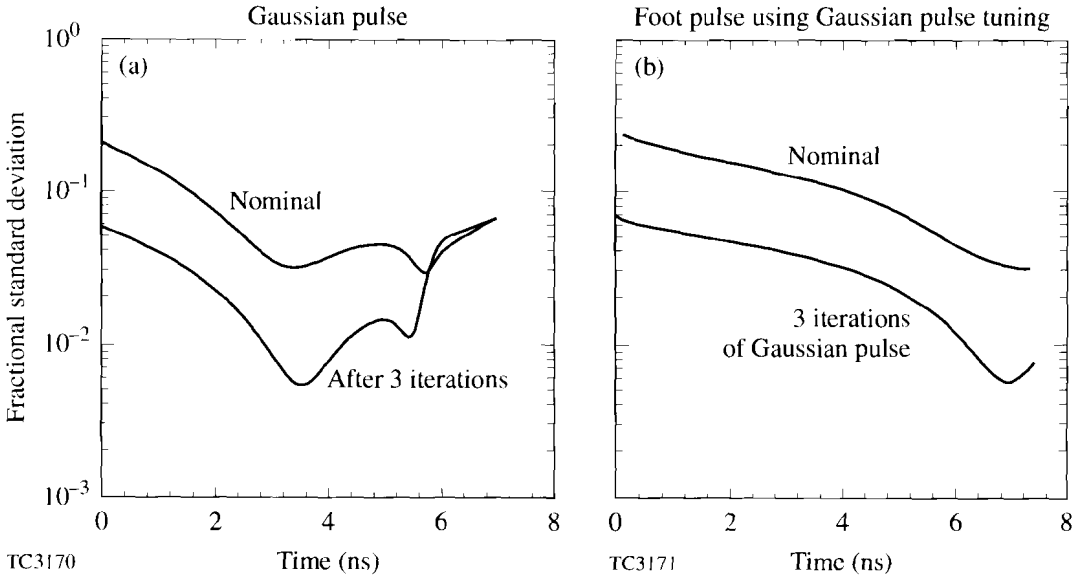

Fig. 52.8
Temporal dependence of the fractional standard deviation when using a Gaussian pulse to obtain the constants in Eq. (2). (a) Gaussian pulse; (b) foot pulse.

foot and main beams. This level of power balance is obtained at the expense of the output beam energy, which is reduced by about 6%. It also requires a 1% measurement accuracy of the UV ouput energy and peak power. The following were not considered in this article: power imbalance caused by uncertainties in the conversion-crystal efficiency, including variations in beam sizes; variations in the transport optics; and beam timing.

ACKNOWLEDGMENT

This work was supported by the U.S. Department of Energy Office of Inertial Confinement Fusion under agreement No. DE-FC03-85DP40200 and by the Laser Fusion Feasibility Project at the Laboratory for Laser Energetics, which is sponsored by the New York State Energy Research and Development Authority and the University of Rochester.

REFERENCES

1. *OMEGA Upgrade Preliminary Design*, edited by R. S. Craxton, Laboratory for Laser Energetics Report DOE/DP 40200-101, University of Rochester (1989), Chap. 4.
2. *Ibid*, p. 2.19.
3. C. P. Verdon, private communication.

1.B Damping of Ion-Acoustic Waves in the Presence of Electron-Ion Collisions

The study of ion-acoustic waves in plasmas has been the subject of considerable interest for the past 30 years.[1–7] Their damping rate plays an important role in establishing the threshold for the onset of stimulated Brillouin scattering, ion-temperature-gradient instability, current-driven ion-acoustic instability, and other drift-wave microinstabilities. In a collisionless plasma the waves are predominantly damped by electron Landau damping for $ZT_e >> T_i$, and by ion Landau damping for $ZT_e \sim T_i$ (where Z is the ionic charge and T is the temperature). The contribution of ion-ion (i-i) collisions to the damping is well understood, and the eigenfrequencies ω have been calculated for arbitrary values of $k\lambda_{ii}$ (where k is the wave number and λ_{ii} is the i-i mean free path), assuming isothermal electrons.[1] Kulsrud and Shen[2] were among the first to calculate the effect of introducing weak e-i collisions. They solved the linearized electron Fokker-Planck (FP) equation by expanding the distribution function about the collisionless result, and showed that for $k\lambda_{ei} >> 1$ (where λ_{ei} is the e-i mean free path) electron collisions give rise to a fractional *reduction* in the Landau damping rate of order $(m_i/Zm_e)/k\lambda_{ei}$. This curious "undamping" effect has been attributed to collisional disruption of the wave-particle resonance. It has since been confirmed by many authors using various models for the collision operator.[3–5] It has even been suggested that such an undamping effect, including possible instability, could be demonstrated experimentally.[5]

Here we present the first calculation of ion-acoustic wave damping based on an analytic solution of the electron FP and cold-ion fluid equations, for arbitrary e-i collisionality (omitting e-e collisions). This has been achieved by developing a reduced form of the FP equation with an (ω, k)-dependent e-i collision frequency. We show that the total damping rate can be accurately obtained by adding a collisional damping rate (arising from thermal diffusion) to a collisionally reduced Landau damping rate (arising from wave-particle interaction). However, despite the collisional disruption of Landau damping, collisional damping itself prevails so that there is no net undamping of the ion-acoustic wave. In fact, as e-i collisions are introduced, the damping rate γ rises monotonically above the collisionless Landau limit γ_L, reaches a peak at $k\lambda_{ei} \sim (Zm_e/m_i)^{1/2}$ (where the thermal-diffusion rate $\approx$ sound-transit rate), and then decreases to zero as $k\lambda_{ei} \rightarrow 0$, as predicted by fluid theory. The undamping effect predicted by previous authors is found to be an artifact of the method used in the derivation of the dispersion relation, which in most cases involved expanding the distribution function about the collisionless limit. Huang, Chen, and Hasegawa[4] realized the problem associated with this approach and adopted the approximate method of splitting the electron-distribution function into collisional and collisionless parts. However, by failing to correctly obtain the contribution from the highly collisional low-velocity part, they also predicted a reduction in the damping rate below γ_L. Dum,[6] who considered this problem in the context of strong turbulence, did indeed find that e-i collisions enhance the damping. However, his equations

were not energy and momentum conserving, so that his results were only valid in the weakly collisional limit (i.e., $k\lambda_{ei} >> 1$). Recently, Bell[7] investigated the effect of *e-i* collisions on sound waves over the range $0 < k\lambda_{ei} < 1$ (i.e., for strong to intermediate collision strength) and found an enhancement in the damping above fluid-theory predictions for $k\lambda_{ei} > 0.01$. He attributed this enhancement to a reduction in the thermal conductivity below the classical Spitzer-Härm[8] (SH) value. In this article we also demonstrate a reduction in the thermal conductivity, and by extending the results to the collisionless limit ($k\lambda_{ei} >> 1$) we show that the effective thermal conductivity approaches the collisionless value calculated by Hammett and Perkins.[9]

We start by assuming a homogeneous plasma where the electrons collide elastically with cold-fluid ions only. Therefore, we neglect *e-i* energy exchange (since $m_e/m_i << 1$),[4] as well as *i-i* collisions. The effect of *e-e* collisions, which is expected to become important for low-Z plasmas, will be considered in a subsequent article. Adopting a perturbation of the electron-distribution function of the form

$$f(x, \mathrm{v}, t) = F_0(v) + \sum_{l=0}^{\infty} f_l(v) P_l(\mu) \exp[-i(\omega t - kx)] , \tag{1}$$

where $\mu = v_x/v$ and $P_l(\mu)$ is the lth Legendre mode, the linearized electron FP equation (defined in the rest frame of the ions) becomes[10]

$$-i\omega f_0 + \frac{ikv}{3} f_1 - \frac{iku_i}{3} v \frac{\partial F_0}{\partial v} = 0 , \tag{2}$$

$$-i\omega f_1 + ikvf_0 + ikv\frac{2}{5} f_2 - \left(\frac{|e|E}{m_e} - i\omega u_i \right) \frac{\partial F_0}{\partial v} = -\nu_1 f_1 , \tag{3}$$

$$-i\omega f_2 + \frac{2}{3} ikvf_1 + \frac{3}{7} ikvf_3 - \frac{2}{3} iku_i v \frac{\partial F_0}{\partial v} = -\nu_2 f_2 , \tag{4}$$

and

$$-i\omega f_l + \frac{l}{2l-1} ikvf_{l-1} + \frac{l+1}{2l+3} ikvf_{l+1} = -\nu_l f_l , \tag{5}$$

for $l > 2$.

The ion velocity u_i and electric field E are first order in the perturbation and

$$F_0(v) = N_e \left(2\pi v_t^2\right)^{-3/2} \exp\left(-v^2 / 2v_t^2\right)$$

is an equilibrium Maxwellian, where N_e is the background electron number density and $v_t = \left(T_e / m_e\right)^{1/2}$ is the electron thermal velocity. The collision operators are given by $\nu_l(v) = \nu(v) l(l+1)/2$, where

$$\nu(v) = 4\pi N_e Z\left(e^2 / m_e\right)^2 \ln\Lambda / v^3$$

is the velocity-dependent *e-i* angular scattering collision frequency, e is the electron charge, and lnL is the Coulomb logarithm.

Substituting Eqs. (5) and (4) into (3) we obtain the following reduced form of the f_1 equation, which includes all contributions from f_2, f_3, ...,

$$ikvf_o - \left(\frac{|e|E}{m_e} - i\omega u_i + \frac{4k^2v^2}{15\nu_2^*}u_i\right)\frac{\partial F_o}{\partial v} = -\nu_1^* f_1 \ . \tag{3a}$$

This reduction has been accomplished by introducing an effective collision frequency $\nu_l^*(v,k,\omega) = \nu_l(v)\left[1 - i\omega/\nu_l(v)\right]H_l(v,k,\omega)$, where the effect of higher-order Legendre modes has been embodied in the continued fraction $H_l(v,k,\omega) = 1 + c_{l+1}/\left(1 + c_{l+2}/...\right)$, with coefficients

$$c_l = 4k^2\lambda^2 / \left[\left(4l^2 - 1\right)\left(l^2 - 1\right)\left(1 - i\omega/\nu_l\right)\left(1 - i\omega/\nu_{l-1}\right)\right] \text{ and } \lambda \equiv v/\nu.$$

(This method of incorporating higher-order Legendre modes has also been successfully applied to the study of thermal filamentation.)[11] For the present analysis of low-frequency waves, setting $\omega = 0$ in ν^* (which leads to a purely real ν^*) has been found to have a negligible effect on the results. The continued fraction converges for all finite $k\lambda$, though a large number of terms are required as $k\lambda$ increases.

The linearized cold-ion continuity and momentum equations are

$$-i\omega n_i + ikN_i u_i = 0, \tag{6}$$

$$-i\omega N_i m_i u_i = ZN_i |e| E + R_{ie}, \tag{7}$$

where $R_{ie} = \left(4\pi m_e / 3\right)\int dv v^3 \nu f_1$ is the *i-e* momentum exchange rate, n_i is the perturbed ion number density, and N_i is its background value. Inserting Eqs. (2) and (3a) into (6) and (7) and assuming quasi-neutrality (i.e., $Zn_i \approx 4\pi\int dv v^2 f_o$) we obtain the dispersion relation

$$\left(\frac{\omega}{kc_s}\right)^2 = \frac{\left(1 + \eta J_4\right)^2}{J_7} - \eta\left(\eta J_1 + \frac{1}{3}\sqrt{\frac{2}{\pi}}\right), \tag{8}$$

where $c_s = (ZT_e/m_i)^{1/2}$ is the isothermal sound speed,

$$J_m = \sqrt{\frac{2}{\pi}}\int_0^\infty dV \frac{V^m \exp\left(-V^2/2\right)}{V^5 - 3\eta\left(1 - i\omega/\nu_1\right)H_1}, \tag{9}$$

$V = v/v_t$, $\eta = i(v_p/v_t)/(k\lambda_t)$ is a collisionality parameter, $v_p = \omega/k$ is the phase velocity, and $\lambda_t = \lambda(v_t)$ is the *e-i* scattering mean free path.

Equation (8) has been solved for $\omega = \omega_r - i\gamma$, and the normalized ion-acoustic damping rate γ/kc_s is plotted in Fig. 52.9 (solid curve) as a function of $k\lambda_{ei}$, for $A = 2Z$ [where A is the atomic mass and $\lambda_{ei} = 3T_e^2/4(2\pi)^{1/2}N_e^4 \ln\Lambda = 3(\pi/2)^{1/2}\lambda_t$]. Starting from the collisionless Landau limit $\gamma_L/kc_s = (\pi Zm_e/8m_i)^{1/2}$ (identified by the arrow on the right-hand side of the figure), we note that introducing weak collisions has the effect of enhancing the damping rate (by about 0.05% for $k\lambda_{ei} = 10^5$). This conclusion is in agreement with the results based on Dum's[6] model (shown by the dashed curve *a* of Fig. 52.9). However, since he neglected compressional heating [third term on the left-hand side of Eq. (2)] and the *i-e* momentum exchange rate [term R_{ie} in Eq. (7)], his dispersion relation becomes $\omega = kc_s/\sqrt{J_7}$, which is valid only for $k\lambda_{ei} >> 1$.

Kulsrud and Shen's[2] cold-ion damping rates are displayed as dashed curve *b* in Fig. 52.9. Their results, which imply a strong reduction in damping, followed by eventual wave growth ($\gamma < 0$), are typical of results based on small $1/k\lambda_{ei}$ expansions about the collisionless limit. Their physical explanation of undamping is that collisions disrupt the wave-particle resonance responsible for Landau damping. We find, however, that although collisions inhibit Landau damping, collisional damping itself prevails.

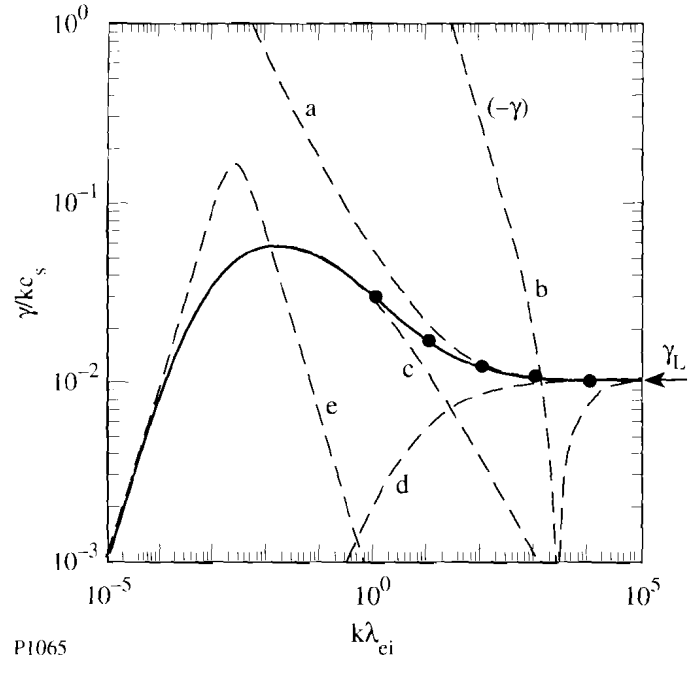

Fig. 52.9
Plots of damping rate of ion-acoustic waves γ/kc_s as a function of $k\lambda_{ei}$, where c_s is the isothermal sound speed, k is the perturbation wave number, and λ_{ei} is the electron-ion mean free path. The solid curve refers to the current FP results; dashed curves refer to models of (a) Dum, (b) Kulsrud and Shen, (c) Bell, (d) collisionally reduced Landau damping, and (e) fluid equations. The arrow on the right-hand side corresponds to the Landau damping rate γ_L/kc_s. Circles are obtained by adding curves *(c)* and *(d)*. Convergence required up to 400 terms in H_1 for the largest value of $k\lambda_{ei}$.

Let us first consider the damping arising solely from collisions. We do this by solving the FP equation in the diffusive limit, which involves truncating the Legendre expansion [Eq. (1)] at $l = 1$ (or simply using $H_1 = 1$), and neglecting the $-i\omega f_1$ term in Eq. (3). Such an approach has been previously adopted by Bell[7] and gives rise to damping rates shown by the dashed curve *c* in Fig. 52.9. This type of damping results predominantly from electrons that diffuse across a distance k^{-1} in a time ω^{-1}. The velocity of these electrons can be estimated by setting $V^5 \sim 3|\eta|$ in the denominator of Eq. (9) and is found to be

$$v \sim v_c = v_t\left[9\left(\pi Z m_e / 2m_i\right)^{1/2} / k\lambda_{ei}\right]^{1/5}$$

To isolate the *collisionless* Landau-damping mechanism, which is dominated by electrons with velocities in phase with the wave (i.e., $v_x \sim v_p$), one would set $\nu = 0$. To include collisional disruption of the wave-particle interaction, we keep ν_l for all $l > 1$ yet set $\nu_1 = 0$. (The latter requirement ensures that there is no damping from thermal diffusion.) The corresponding damping rates, as shown in curve *d* in Fig. 52.9, fall below the collisionless Landau limit.

We find that the total damping rate can be obtained by adding the previously described "collisional damping" and "collisionally reduced, Landau-damping" rates. This is shown (as circles) in Fig. 52.9 over the range $1 < k\lambda_{ei} < 10^5$, where we find agreement with the full FP result to better than three significant figures. The reason for the successful superposition of both damping processes is that they originate from distinct regions in electron velocity space. This is illustrated by plotting contours in Figs. 52.10(a)–52.10(c) of the imaginary part of $f(v_x, v_\perp)$ (which is responsible for γ) as a function of v_x and

$$v_\perp = \left(v^2 - v_x^2\right)^{1/2}$$

at $k\lambda_{ei} = 10^5$. Figure 52.10(a) shows the result for collisional damping only. The dashed curve identifies electrons traveling with a velocity $v = v_c \approx 0.07 v_t$, which are the ones that can diffuse a distance $\sim k^{-1}$ in a time ω^{-1}. Since these dominate the collisional damping process, Im(f) has its maximum near $v = v_c$, with a peak in the direction of the heat flow. Figure 52.10(b) depicts the distribution for the collisionally reduced, Landau-damping mechanism, with $\nu_1 = 0$. The electron distribution is now concentrated along the dashed line $v_x = v_p$, where the electrons are in phase with the wave. However, unlike the classical collisionless case, where Im(f)is independent of $v_\perp$, we find that Im(f) is small near the origin. This is caused by strong collisional disruption of the wave-particle resonance, when the collision frequency $\nu(v) \propto 1/v^3$ becomes large. By comparing with the collisionless result (not shown), we also find a general broadening of the distribution about $v_x = v_p$. When both damping processes are operative, as shown in Fig. 52.10(c), one can still clearly identify the distinctive features of each.

Let us now consider the collisional regime $k\lambda_{ei} < 1$. Dashed curve *e* in Fig. 52.9 shows the classical damping rate derived from the fluid equations, neglecting

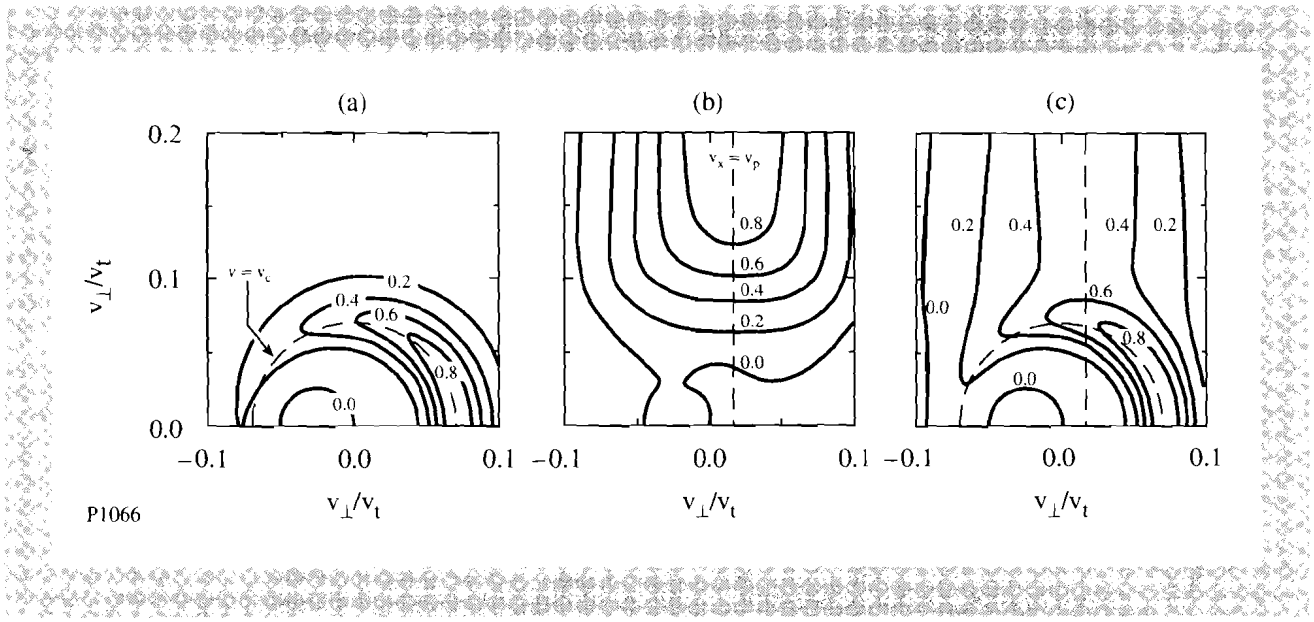

Fig. 52.10
Normalized contour plots of the perturbed distribution function Im(f) (in intervals of 0.2) as a function of v_x and $v_\perp$, for (a) collisional damping, (b) collisionally reduced Landau damping, and (c) full damping (for $k\lambda_{ei} = 10^5$).

electron viscosity.[12] As expected, when $k\lambda_{ei} \to 0$, fluid and kinetic results are in agreement. In the fluid limit, the maximum γ is found to occur when the ratio of the thermal-diffusion rate to the sound-transit rate is of order unity, i.e., $2k^2\kappa_{SH}/3n_e k c_s \sim k\lambda_{ei}(m_i/Zm_e)^{1/2} \sim 1$, where κ_{SH} is the SH thermal conductivity. When $k\lambda_{ei}(m_i/Zm_e)^{1/2} > 1$, electron kinetic effects start to dominate and fluid theory breaks down. Associated with this breakdown is a reduction in the effective thermal conductivity $\kappa \equiv -q/ikT_{FP}$ [where $q = (2\pi m_e/3)\int dv v^5 f_1$, and $T_{FP} = (4\pi m_e/N_e)\int dv\left(v^4/3 - v^2 v_t^2\right) f_0$] relative to κ_{SH}, as shown by the solid curve in Fig. 52.11(a). This heat flow inhibition, first pointed out by Bell[7] [dashed curve *a* in Fig. 52.11(a)], is a consequence of the decoupling between the relatively collisionless heat-carrying electrons and the bulk thermal-electron population. In the $k\lambda_{ei} >> 1$ limit our result agrees with the heat-flow coefficient obtained by Hammett and Perkins[9] [dashed curve *b* in Fig. 52.11(a)] for a collisionless plasma. It should be noted that the effective conductivity is actually complex over a wide range of $k\lambda_{ei}$, as shown by the phase plot of κ in Fig. 52.11(b).

In summary, we have developed a simplified form of the FP equation that is valid for arbitrary *e-i* collisionality, through the introduction of a generalized collision frequency $\nu^*(v,k,\omega)$. We have demonstrated that the effective damping of a sound wave can be treated as a linear combination of a purely collisional damping and a collisionally reduced Landau damping. In contrast to results in several published works, the introduction of *e-i* collisions increases the damping above the collisionless Landau value.

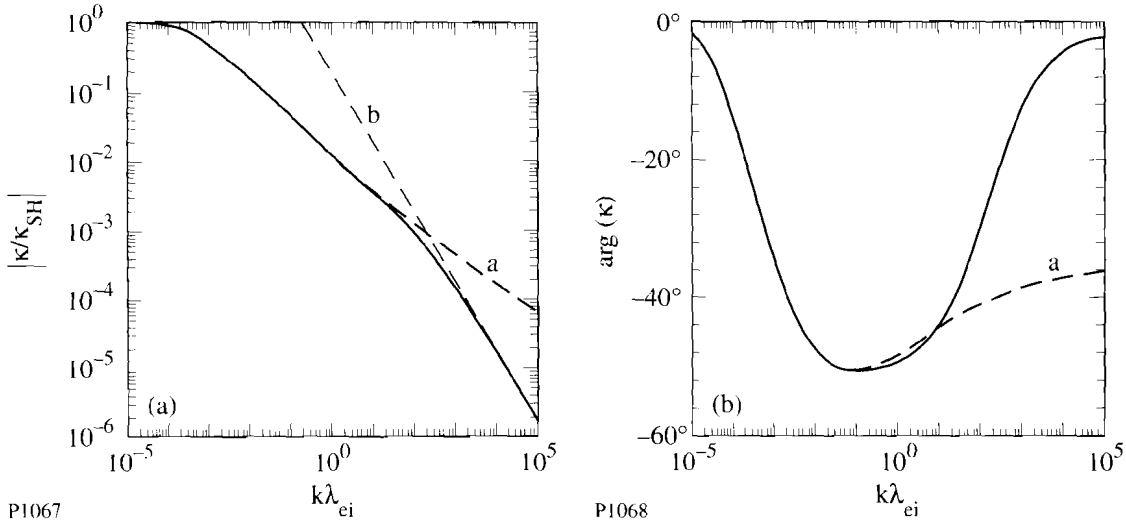

Fig. 52.11
Plots of (a) $|\kappa/\kappa_{SH}|$ and (b) $\arg(\kappa)$ as a function of $k\lambda_{ei}$, where κ and κ_{SH} are the effective and Spitzer-Härm thermal conductivities, respectively. The solid curve refers to the current FP results; dashed curves refer to models of (a) Bell and (b) Hammett and Perkins.

ACKNOWLEDGMENT

This work was supported by the U.S. Department of Energy Office of Inertial Confinement Fusion under agreement No. DE-FC03-85DP40200 and by the Laser Fusion Feasibility Project at the Laboratory for Laser Energetics, which is sponsored by the New York State Energy Research and Development Authority and the University of Rochester.

REFERENCES

1. D. Bhadra and R. K. Varma, Phys. Fluids **7**, 1091 (1964); M. Ono and R. M. Kulsrud, Phys. Fluids **18**, 1287 (1975); C. J. Randall, Phys. Fluids **25**, 2231 (1982).
2. R. M. Kulsrud and C. S. Shen, Phys. Fluids **9**, 177 (1966).
3. B. Buti, Phys. Rev. **165**, 195 (1968); R. S. B. Ong and M. Y. Yu, J. Plasma Phys. **3**, 425 (1969); R. J. Stéfant, Phys. Fluids **14**, 2245 (1971).
4. T.-Y. Huang, L. Chen, and A. Hasegawa, Phys. Fluids **17**, 1744 (1974). The proper solution of their Eq. (15), to lowest order in $1/D(v)$, is the result they give in Eq. (23) plus an added ψ-independent term $-\alpha F_e^{\,o} v/6Dv_\varphi$. The resultant density perturbation, from their low-velocity region, no longer vanishes.
5. J. R. Jasperse and B. Basu, Phys. Rev. Lett. **58**, 1423 (1987); B. Basu and J. R. Jasperse, Phys. Rev. A **38**, 3785 (1988).
6. C. T. Dum, Phys. Rev. Lett. **35**, 947 (1975).
7. A. R. Bell, Phys. Fluids **26**, 279 (1983).
8. L. Spitzer and R. Härm, Phys. Rev. **89**, 977 (1953).

9. G. W. Hammett and F. W. Perkins, Phys. Rev. Lett. **64**, 3019 (1990).

10. I. P. Shkarofsky, T. W. Johnston, and M. P. Bachynski, *The Particle Kinetics of Plasmas* (Addison-Wesley, London, 1966); T. W. Johnston, J. Math. Phys. **7**, 1453 (1966).

11. E. M. Epperlein and R. W. Short, Phys. Fluids B **4**, 2211 (1992).

12. P. M. Morse and H. Feshbach, *Methods of Theoretical Physics* (McGraw-Hill, New York, 1953), Part I, p. 268.

Section 2
ADVANCED TECHNOLOGY DEVELOPMENTS

2.A Optical Nonlinearities in High-Temperature Superconductors

Superconductor photoexcitation studies have been a subject of intense investigations for the last 20 years.[1] Early experiments were performed on metallic superconductors, using nanosecond and picosecond laser pulses, and were focused on the dynamics of the photon-induced superconducting-to-normal transition. It has been demonstrated experimentally[2,3] and explained theoretically[4] that under moderately weak optical excitation a superconducting thin film undergoes a transition into a nonequilibrium (transient) intermediate state, which is characterized by the coexistence of spatially separated superconducting and normal domains in the film. The dynamics of the intermediate state were found to be on a picosecond time scale,[3,5] contrary to a slow, heat-diffusion-related bolometric response observed in the films under strong laser excitation. The discovery of high-temperature superconductors (HTS) prompted a new series of transient photoexcitation measurements.[6–10] It was observed that, unlike low-T_c materials, the response of optically thick $YBa_2Cu_3O_{7-x}$ (YBCO) film was primarily bolometric with a small nonthermal (nonequilibrium) component. The relative magnitude of the nonthermal component was enhanced and could be as fast as tens of picoseconds for ultrathin films under moderate excitation.[10]

Very recently, a different class of laser-excitation experiments has been performed to investigate transient nonequilibrium properties of both low- and high-T_c superconducting materials,[11–19] namely, femtosecond pump-probe measurements. In particular, femtosecond time-resolved measurements of the

differential reflectivity $\Delta R/R$ have been performed at 2 eV for various temperatures. Results interpreted using the Fermi smearing model, which was used previously to explain the dynamics of $\Delta R/R$ in metals,[20,21] indicate a different position of the Fermi level (E_F) in the oxygen-p band of oxygen-rich and oxygen-poor samples at room temperature. On the other hand, the picosecond response of $\Delta R/R$, measured on optically thick YBCO films at temperatures below T_c, has been interpreted as a direct indication of the relaxation dynamics of quasiparticles[16,17] and/or the order parameter.[18] The very recent results of Reitze *et al.*[19] imply, however, that a detailed energy band structure also has to be taken into account if any physical significance is to be assigned to these relaxation rates measured at optical frequency.

In this article we present a series of femtosecond reflectivity measurements on YBCO films. For the first time, we discuss in detail the dependence of $\Delta R/R$ on probing laser frequency, pumping laser intensity, and bias electric current. In particular, our study provides information on the nature of the transient optical response in optically thin and thick YBCO films under weak and strong laser excitations, as well as on the shift of the Fermi level between the oxygen-rich and oxygen-poor samples.

This article is organized as follows: First we provide a brief survey of the relation between the optically measured $\Delta R/R$ and the change of the dielectric permittivity $\Delta\varepsilon$ for optically thick and thin films, in connection with the models commonly used to explain the change of optical and electric properties of HTS materials. We then describe the sample fabrication and experimental arrangement. Next, we discuss our experimental results and compare them with existing models, and finally, we present our conclusions and suggestions for future investigations.

Background

The normal-incidence reflectivity R for an optically thick sample can be described by

$$R = \frac{(n-1)^2 + k^2}{(n+1)^2 + k^2} , \tag{1}$$

where n and k are the real and imaginary parts of the index of refraction. The real and imaginary parts of the dielectric permittivity (ε_1 and ε_2, respectively) are related to n and k by

$$\varepsilon_1 = n^2 - k^2 , \tag{2}$$

$$\varepsilon_2 = 2nk . \tag{3}$$

Therefore, using Eqs. (1) to (3), $\Delta R/R$ can be simply expressed as

$$\Delta R / R = a\Delta\varepsilon_1 + b\Delta\varepsilon_2 , \tag{4}$$

where a and b are determined by the unperturbed values of ε_1 and ε_2.

For most of the semiconducting materials, $a >> b$ and $\Delta R/R$ is thus dominated by $\Delta\varepsilon_1$. In contrast, for metals, $a << b$ and $\Delta R/R$ is essentially proportional to $\Delta\varepsilon_2$. Using unperturbed values of ε_1 and ε_2 obtained from ellipsometry measurements,[22] we have calculated the values of a and b for $YBa_2Cu_3O_{6.85}$ at the energy of 2 eV and found them to be 0.16 and 0.25, respectively. Thus for YBCO, $\Delta R/R$ could in principle depend strongly on both $\Delta\varepsilon_1$ and $\Delta\varepsilon_2$. However, one must remember that the magnitudes of $\Delta\varepsilon_1$ and $\Delta\varepsilon_2$ themselves can vary substantially, making $\Delta R/R$ dominated by $\Delta\varepsilon_1$ if $\Delta\varepsilon_1 >> \Delta\varepsilon_2$ or $\Delta\varepsilon_2$ if $\Delta\varepsilon_1 << \Delta\varepsilon_2$.

The dependence of the optical reflectivity on sample properties changes when the measurement is performed on an optically thin film, fabricated on a non-index-matched substrate. In this case, multiple reflections from the sample-substrate interface must be taken into account. As a result, the relation between $\Delta R/R$ and $\Delta\varepsilon$ is much more complicated than that shown in Eq. (4). It is very important to note that when $\Delta\varepsilon_1$ dominates the $\Delta R/R$ signal, the sign of $\Delta R/R$ depends on the sample thickness d, whereas when $\Delta\varepsilon_2$ dominates the $\Delta R/R$ signal, the sign (either positive or negative) of $\Delta R/R$ is independent of d. In particular, when $\Delta R/R$ measured for samples with different d's is dominated by $\Delta\varepsilon_1$, $\Delta R/R$ changes sign for a thickness difference Δd given by the relation $\Delta d/\lambda = 1/(4n)$. For 2-eV optical-excitation energy ($\lambda = 620$ nm), the calculated Δd for YBCO is ~75 nm, which is within the range of thickness variations of the samples used in our study.

The Fermi smearing model is most commonly used in explaining the transient ΔR and ΔT signals in d-band metals and YBCO-related HTS materials, which are in the normal state. In this model, the pump pulse heats carriers (either electrons or holes) and modifies the electronic occupancy near the Fermi level on a time scale typically shorter than the pulse width. This "smearing" decreases (increases) the occupancy of states below (above) E_F. Thus, a probe monitoring the interband transition from the filled d-band to the p-states below (above) E_F measures a positive (negative) $\Delta\varepsilon_2$.

When the ambient temperature is cooled down below T_c, the free-carrier density of states in the superconductor is modified substantially. According to the BCS theory, in the superconducting state electrons form boson-like Cooper pairs, which occupy a single energy level, separated from E_F by the superconducting energy gap Δ, while unpaired, excited electrons (quasiparticles) occupy a continuum of states, starting Δ above E_F. The 2Δ gap is temperature dependent and, at a given temperature T below T_c but above 0 K, only a fraction $f_C(T)$ of the total number of free carriers forms Cooper pairs, while the rest $(1-f_C)$ remain as quasiparticles. Treating the superconducting condensate and normal electron gas as separate conducting "fluids,"[23] one can obtain ε of the superconducting sample below T_c as

$$\varepsilon = (1 - f_C)\varepsilon_D + f_C\varepsilon_C + \varepsilon_H \ , \tag{5}$$

where ε_D, ε_C, and ε_H are the contributions from the quasiparticles (based on the Drude model), the Cooper pairs, and the high-frequency interband (e.g., d→p) transitions, respectively.

Under optical illumination the thermal equilibrium between the superconducting condensate and quasiparticles is disturbed (often very strongly), since photons with energies >>2Δ can break Cooper pairs and create quasiparticles. The absorption of a single, 2-eV photon in YBCO creates, through the cascading processes of carrier-carrier and carrier-phonon scattering, approximately 100 quasiparticles with energies widely distributed above 2Δ.[24] Thus, even a relatively weak optical excitation leads to highly nonequilibrium transient Cooper-pair/quasiparticle distributions.

As we mentioned previously, the situation is the most complicated for a relatively weak perturbation (typically 1 μJ/cm^2 to 5 μJ/cm^2 at 2 eV), since it can lead to the nonequilibrium intermediate state, resulting in the sample partitioning into separate superconducting and normal regions. Under such a condition, the superconductor is in a resistive state, which is, however, thermodynamically different from the normal (nonsuperconducting) state. According to the Elesin theory,[4] the intermediate state is stationary only for a particular excitation power that lies within the region where the energies of both superconducting and normal phases are equal. For perturbations different than critical, the intermediate state is nonstationary, with the dynamics directly related to the temporal dependence of the excitation pulse.[3] The superconducting/normal region boundaries move toward the superconducting state (decreasing the volume of this phase) for a perturbation above critical and toward the normal phase in the opposite case. The intermediate state was found to be an intrinsic feature of optically driven nonequilibrium metallic superconductors and is expected to exist in HTS materials.

Finally, very intense (>>10 μJ/cm^2) optical excitation of superconductors (both metallic and HTS) always results in a thermally induced transition to the normal state. The overall response is slow and can be explained using the bolometric (thermal-diffusion) model.

Experimental Procedures

A number of epitaxial YBCO films with thicknesses from 80 nm to 300 nm have been grown on $SrTiO_3$ single crystals by *in-situ* rf magnetron sputtering.[25] The films typically exhibited about 1.5-K-wide (10% to 90%) resistive superconducting transitions, with zero resistivity, T_c between 87 K (YBCO-I: 200-nm thick) and 83 K (YBCO-II: 80-nm thick). In addition, we have tested a 200-nm-thick, laser-ablated sample (YBCO-III) fabricated at the New York State Institute on Superconductivity,[26] and a 280-nm-thick sputtered film (YBCO-IV) provided by the Westinghouse Science and Technology Center.[27] The superconducting transition for the YBCO-IV sample was 0.5 K wide and its T_c was 89.5 K. For the sample YBCO-III, T_c was 86.5 K. All the tested films exhibited critical-current densities J_c greater than 10^6 A/cm^2 at liquid-nitrogen temperature. A partially oxygen-depleted YBCO sample (YBCO-V) was also fabricated. The film was deposited together with YBCO-I, but after deposition it was furnace annealed at 500°C for 20 min in pure Ar atmosphere. As a result, its T_c was lowered to 27 K, consistent with a decrease of the oxygen content of YBCO to about 6.45. For transport-current measurements, a film fabricated in the same run as the YBCO-IV sample was patterned into a 50-μm-wide and about

1-mm-long microbridge using a laser-ablation method.[28] The patterning lowered the bridge J_c to about 10^5 A/cm^2 at 77 K.

Femtosecond measurements were performed using a colliding-pulse, mode-locked (CPM) laser, which was either unamplified or amplified by a copper-vapor laser. Depending on the amplification arrangement, the CPM provided a train of pulses with either a high repetition rate (~100 MHz) and low energy (~0.1 nJ/pulse), or at moderate repetition rate (~8.5 KHz) and high energy (>1 μJ/pulse). This arrangement allowed us to change the pump laser intensity I_p for 2-eV photons by more than three orders of magnitude, as well as to use a different wavelength probe pulse selected from a white-light continuum. Time-resolved $\Delta R/R$ measurements have been performed with a temporal resolution of 100±20 fs, using a conventional pump-probe arrangement. Lock-in and differential-detection techniques were used to obtain a good signal-to-noise ratio. The polarization of the weak (probe) beam was rotated by 90° relative to that of the pump beam to reduce the coherent artifact. Both beams were focused on the sample using a 5-cm lens, resulting in a focusing spot size of 40±10 μm. The measurements have been performed in a temperature-controlled, continuous-flow optical cryostat in the temperature range between 12 K and 300 K.

Results and Discussion

1. Room-Temperature Measurements

Figure 52.12 illustrates the temporal dependence of the $\Delta R/R$ signal, measured on the YBCO-III sample at room temperature. The probe photon energy was

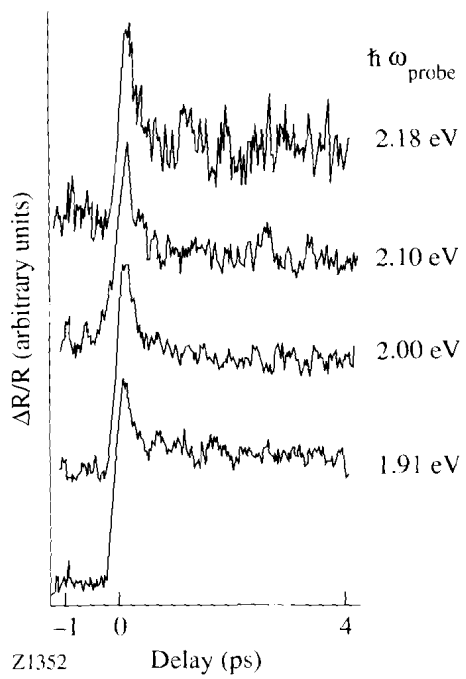

Fig. 52.12
Normalized changes in reflectivity $\Delta R/R$ (~10^{-4}) measured on the YBCO-III sample at room temperature using the probe photon energies indicated in the figure.

varied from 1.91 eV to 2.25 eV (the 2.25-eV data are not shown in Fig. 52.12), while the pump photon energy was kept constant at 2 eV with I_p about 10 μJ/cm^2. We note that for all probe photon energies, $\Delta R/R$ exhibits a similar behavior—a positive pulse-width-limited rise, followed by a fast decrease, and then a long-lasting (several-nanoseconds) plateau. Following Refs. 12 and 14, such a "bolometric" response can be simply explained by the smearing of the electron (hole) distribution near E_F, which in the case of YBCO lies in the oxygen-p band. The positive $\Delta R/R$ at all wavelengths results from the change of $\Delta\varepsilon_2$ with probing of unoccupied hole states below E_F. A very similar behavior to that presented in Fig. 52.12 was also obtained for sputtered films (YBCO-I sample).

At 2 eV, $\Delta R/R$ was positive for all our samples with thickness from 80 nm to 300 nm, implying that $\Delta\varepsilon_2 >> \Delta\varepsilon_1$. Therefore, $\Delta R/R$ is proportional to $\Delta\varepsilon_2$ and its behavior can indeed be explained by the Fermi smearing model; in this sense, YBCO exhibits a behavior similar to typical d-band metals, such as Cu. We have also observed that the temporal response of $\Delta R/R$ at 2 eV has little dependence on pump-pulse intensity from 0.3–100.0 μJ/cm^2. Another important observation is that since in our experiments $\Delta\varepsilon_2$ does not show a sign reversal in the energy range from 1.91 eV to 2.25 eV, E_F must be at least 2.25 eV above the Cu-d^9/d^{10} bands. This result, which is a direct consequence of the Fermi smearing model, is inconsistent with earlier findings of Kazeroonian *et al.*,[14] who, from the dependence of $\Delta R/R$ at 2 eV on Pr-doping concentration, concluded that E_F was about 2 eV above the d-band of YBCO.

By contrast, $\Delta R/R$ measured at room temperature on the partially deoxygenated YBCO-V sample showed (see Fig. 52.13) a negative change at 2 eV. The initial decrease is again pulse-width limited, but it is then followed by a very fast (~300-fs) recovery. The sign change at 2 eV for oxygen-poor YBCO films was

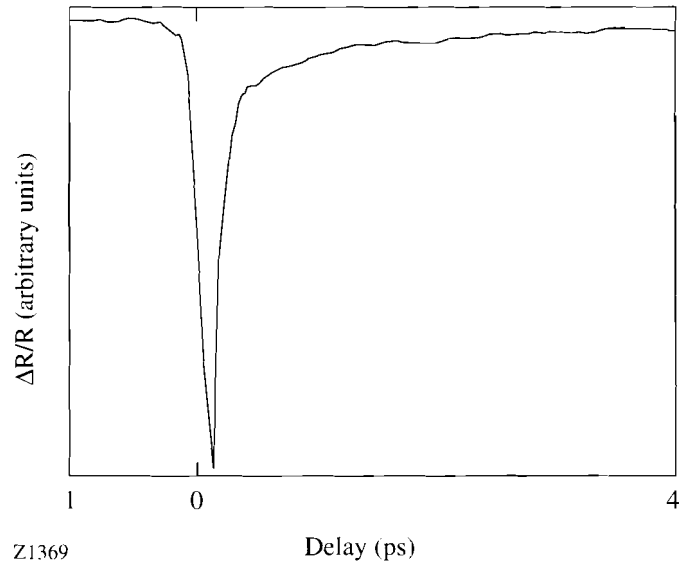

Fig. 52.13
Normalized $\Delta R/R$ measured on the YBCO-V (partially oxygen depleted) sample at room temperature using a 2-eV probe photon energy.

previously observed by Brorson *et al.*[12] and explained in the framework of the Fermi smearing model. The sign change was accounted for by a shift of the Fermi level, associated with a drastic change in the free-carrier concentration between the oxygen-rich and oxygen-poor films. Following again the Fermi smearing model, our results imply that in YBCO E_F must shift down (using the hole picture) by at least 250 meV when the sample oxygen deficiency decreases from above 6.9 to about 6.45.

2. Low-Temperature Measurements

Figure 52.14 shows $\Delta R/R$ at 2 eV measured at $T = 25$ K on two superconducting samples when a weak excitation ($I_p \approx 1$ μJ/cm^2) is used. The negative $\Delta R/R$ followed by a moderately fast (several-picoseconds) recovery, presented in Fig. 52.14(a), was measured on the 280-nm-thick YBCO-IV film and is very similar to results obtained on optically thick (from 250-nm- to 500-nm-thick) samples by others.[16–19] By contrast, in Fig. 52.14(b) we observe a *positive* $\Delta R/R$ with similar temporal response, obtained on the optically thin YBCO-II sample. A positive $\Delta R/R$ was also found in Ref. 19 for a 140-nm-thick YBCO sample ($T_c \approx 91$ K). We believe that the observed $\Delta R/R$ sign reversal between the optically thick and thin samples, which was not present at room temperature, is caused by a thin-film effect and suggests that $\Delta\varepsilon_1 >> \Delta\varepsilon_2$. Therefore, at $T < T_c$, it is $\Delta\varepsilon_1$ and not $\Delta\varepsilon_2$ that dominates $\Delta R/R$ at 2 eV. The correct sign of $\Delta\varepsilon_1$ can be only obtained from an optically thick film and is indeed negative under the previously mentioned experimental conditions.

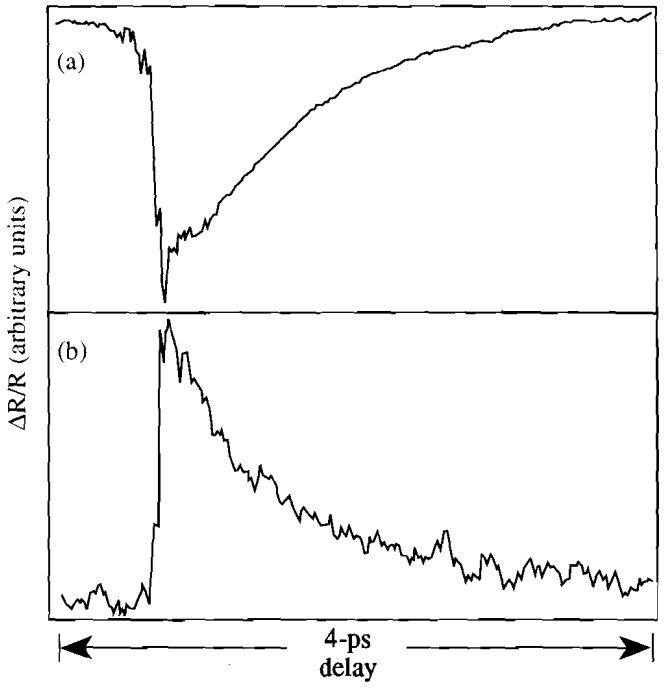

Fig. 52.14
Normalized $\Delta R/R$ ($\sim 10^{-4}$) measured on (a) YBCO-IV and (b) YBCO-II samples at $T = 25$ K using a 2-eV probe photon energy. The pump intensity was ~1 μJ/cm^2.

It was already noticed by Reitze *et al.*[19] that the amplitude of $\Delta R/R$ for YBCO films is about two orders of magnitude larger than that estimated from $\Delta\varepsilon_{1D}$ [change in the real part of the Drude component in Eq. (5)]. In fact, at I_p = 1 μJ/cm^2 the estimated density of photoexcited quasiparticles[24] δN_Q is ~4×10^{19} cm^{-3}, which is only a small fraction of the YBCO total density of free carriers. Thus, under such a weak excitation, the superconducting film may not be driven entirely to the normal state and the contribution from $\Delta\varepsilon_{1C}$ cannot be neglected. Breaking only a fraction of the Cooper pairs causes a reduction of the imaginary part of the conductivity (σ_2) and, correspondingly, a positive $\Delta\varepsilon_1$, since $\Delta\varepsilon_1 = -4\pi\Delta\sigma_2/\omega$. Obviously, this is not consistent with the experimentally observed negative $\Delta\varepsilon_1$, indicating that in YBCO the measured $\Delta R/R$ cannot be explained by a simple two-fluid model and a more advanced model that includes the material's band structure must be developed.

It is worth noting that this completely different behavior of $\Delta R/R$ observed for weakly excited superconducting YBCO may be associated with the existence of the intermediate state, which was described previously. In this case, the optically measured signal should consist of a mixed response from both the superconducting state and the normal state, leading to a complicated behavior of $\Delta\varepsilon$. The existence of the transient intermediate state in optically excited YBCO needs, however, a solid experimental confirmation, before any conclusions about its influence on the optical reflectivity can be made.

Figure 52.15 presents $\Delta R/R$ obtained at T = 12 K for the YBCO-I sample under strong 2-eV optical excitation ($I_p \approx 20$ μJ/cm^2). The response consists of a sharp, but time-resolved peak, followed by a long plateau, and is very similar to that observed at room temperature (see Fig. 52.12). We want to stress that for pump intensities ranging from ~10 μJ/cm^2 up to 100 μJ/cm^2 the behavior shown in Fig. 52.15 was characteristic of all our optically thin and thick YBCO samples in the entire temperature range from well below T_c up to room temperature.

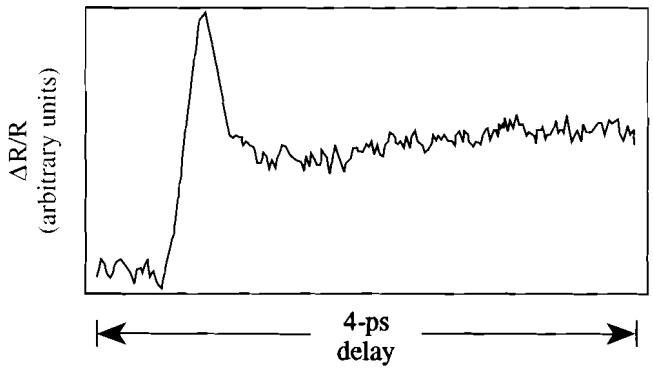

Z1411

Fig. 52.15
Normalized $\Delta R/R$ (~10^{-3}) measured on the YBCO-I sample at T = 12 K using a 2-eV probe photon energy. The pump intensity was ~20 μJ/cm^2.

We believe that under intense laser excitation ($\delta N_Q \sim 10^{21}$ cm^{-3}—of the order of the total free-carrier concentration in YBCO) YBCO undergoes a transition to the normal state.[29] Thus, all the Cooper pairs are destroyed, leaving only the $\Delta\varepsilon_D$ and $\Delta\varepsilon_H$ contributions to the measured $\Delta R/R$. The long-lasting plateau is the signature of a bolometric, heat-diffusion-determined response. This latter result is very similar to that presented previously. It is also consistent with the nanosecond photovoltage response measured for similar laser intensities.[29] On the other hand, the fact that the magnitude of the $\Delta R/R$ peak value (Fig. 52.15) is increased as compared to that measured at room temperature (Fig. 52.12) implies additional contribution from $\Delta\varepsilon_D$; in other words, from photoexcited nonequilibrium quasiparticles.

In a separate series of measurements we have investigated the impact of the electric current on the femtosecond reflectivity of YBCO. Figure 52.16 shows our preliminary data obtained under weak laser excitation ($I_p \approx 1$ μJ/cm^2) on a dc-current-biased, 50-μm-wide superconducting microbridge patterned from the YBCO-IV sample. Figures 52.16(a)–52.16(c) present the $\Delta R/R$ traces measured below J_c, while $\Delta R/R$ in Fig. 52.16(d) was taken above J_c. We note that the curves for $J < J_c$ are very similar to that on Fig. 52.14(a) and their

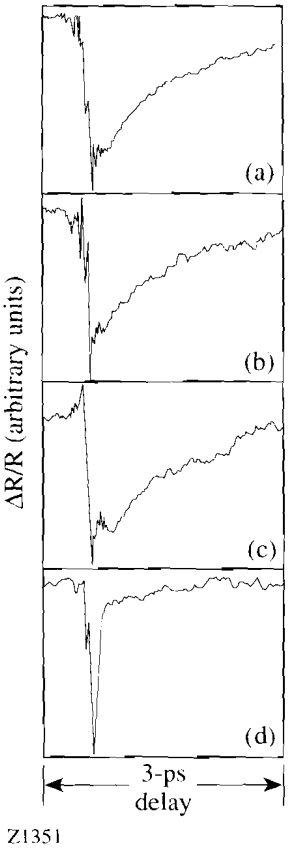

Fig. 52.16
Normalized $\Delta R/R$ measured with a 2-eV probe on the YBCO-IV microbridge biased by the following levels of electric current: (a) 0, (b) 1.5 mA, (c) 6 mA, and (d) 10 mA. The critical current of the microbridge was 8 mA. The temperature was about 72 K and the pump intensity was ~1 μJ/cm^2.

characteristic decay times change slightly with increasing the bias current. On the other hand, the decay time shows a very abrupt decrease when J exceeds J_c. This behavior appears to be correlated with the onset of nonsuperconductivity in YBCO, since earlier femtosecond time-resolved transmission measurements[18] also showed that the decay time drops very abruptly when temperature is increased to T_c. Most interestingly the very fast (negative) response of $\Delta R/R$ shown in Fig. 52.16(d) for $J > J_c$ is very similar to that presented in Fig. 52.13 for the oxygen-poor sample at room temperature, and is completely different from that in a photo-excited *nonequilibrium* normal state (Fig. 52.15). A more detailed discussion of experiments performed on the current-carrying YBCO strips will be presented in a separate publication.

Conclusions

Our results obtained at room temperature provide quantitative information on the position of the Fermi level in YBCO with different oxygen contents. We have found that in superconducting YBCO, E_F must be at least 2.25 eV above the Cu-d^9/d^{10} bands. Simultaneously, there is a large (>250-meV) energy difference between the positions of E_F in the oxygen-rich and oxygen-poor samples. These conclusions are a direct consequence of the Fermi smearing model, which has been generally accepted to explain experimental data for d-band metals, as well as for HTS materials at room temperature.

Measurements performed at temperatures below T_c indicate that in YBCO the optical response, associated with nonequilibrium properties of quasiparticles and Cooper pairs, is strongly dependent on the intensity of optical excitation. Under strong excitation, the temporal dependencies of $\Delta R/R$ in optically thin and thick films are essentially the same and follow those measured at room temperature. In both cases, $\Delta R/R$ is dominated by $\Delta\varepsilon_2$ and the response is primarily bolometric. A completely different behavior is observed for weakly excited films. The $\Delta R/R$ signal exhibits a pulse-width-limited rise, followed by a few-picosecond-long decay, but its sign depends on the film thickness and is negative for optically thick samples. The thickness-dependent sign change in the $\Delta R/R$ signal below T_c indicates that $\Delta R/R$ is dominated by $\Delta\varepsilon_1$. However, its negative sign and relatively large magnitude (measured for the optically thick samples) cannot be explained by the simple two-fluid model. Therefore, more advanced models, based on a detailed material band structure and nonequilibrium quasiparticle/Cooper-pair dynamics, should be developed.

$\Delta R/R$ measurements performed on dc-current-biased superconducting samples showed that YBCO optical responses from current-generated and photoexcited resistive states are different and cannot be easily understood using the existing models. More detailed experiments are necessary to fully characterize the optical properties of current-carrying superconducting films. In particular, it would be desirable to perform simultaneous optical and electrical transient measurements, in which the change in optical reflectivity and the transient voltage generated during the superconducting-resistive transition in the film are measured simultaneously. These measurements should allow us to directly observe the dynamics of the photogenerated superconducting-normal transition and reveal the possible role played in this process by the intermediate state.

ACKNOWLEDGMENTS

The authors would like to thank D. H. Reitze for insightful discussions. We also thank J. P. Zheng and H. S. Kwok from the New York State Institute on Superconductivity for providing the YBCO-III sample, and J. R. Gavaler from the Westinghouse Science and Technology Center for the YBCO-IV sample. This work was supported by the Army Research Office grant DAAL03-92-G-0202. Additional support was provided by the sponsors of the Laser Fusion Feasibility Project at the Laboratory for Laser Energetics.

REFERENCES

1. See, e.g., A. Gilabert, Ann. Phys. Fr. **15**, 255 (1990).
2. G. A. Sai-Halasz *et al.*, Phys. Rev. Lett. **33**, 215 (1974).
3. R. Sobolewski, D. P. Butler, T. Y. Hsiang, C. V. Stancampiano, and G. A. Mourou, Phys. Rev. B **33**, 4604 (1986).
4. See, e.g., V. F. Elesin and Yu. V. Kopaev, Sov. Phys. Usp. **24**, 116 (1981).
5. X.-H. Hu, T. Juhasz, and W. E. Bron, Appl. Phys. Lett. **59**, 3333 (1991).
6. W. R. Donaldson, A. M. Kadin, P. H. Ballentine, and R. Sobolewski, Appl. Phys. Lett. **54**, 2470 (1989).
7. H. S. Kwok *et al.*, Appl. Phys. Lett. **54**, 2473 (1989).
8. E. Zeldov *et al.*, Phys. Rev. B **39**, 9712 (1989).
9. A. Frenkel *et al.*, J. Appl. Phys. **67**, 3054 (1990).
10. L. Shi *et al.*, Appl. Phys. Lett. **61**, 489 (1992).
11. S. D. Brorson *et al.*, Phys. Rev. Lett. **64**, 2172 (1990).
12. S. D. Brorson *et al.*, Solid State Commun. **74**, 1305 (1990).
13. D. W. Face *et al.*, IEEE Trans. Magn. **27**, 1556 (1991).
14. A. S. Kazeroonian *et al.*, Solid State Commun. **78**, 95 (1991).
15. J. M. Chwalek *et al.*, Appl. Phys. Lett. **57**, 1696 (1990).
16. S. G. Han *et al.*, Phys. Rev. Lett. **65**, 2708 (1990); S. G. Han *et al.*, Phys. Rev. Lett. **67**, 1053 (1991).
17. S. G. Han *et al.*, IEEE Trans. Magn. **27**, 1548 (1991).
18. G. L. Eesley *et al.*, Phys. Rev. Lett. **65**, 3445 (1990); G. L. Eesley *et al.*, Phys. Rev. Lett. **67**, 1054 (1991).
19. D. H. Reitze *et al.*, to be published in Physical Review B.
20. G. L. Eesley, Phys. Rev. B **33**, 2144 (1986).
21. R. W. Schoenlein *et al.*, Phys. Rev. Lett. **58**, 1680 (1987).
22. D. E. Aspnes and M. K. Kelly, IEEE J. Quantum Electron. **25**, 2378 (1989).
23. This description may not be totally accurate for HTS materials; however, there is no doubt that in YBCO hole pairs form the superconducting condensate and the two-fluid model is general enough to apply for HTS materials in equilibruim.

24. We assumed that the quasiparticle multiplication factor is 100, which is similar to that used in Ref. 16.

25. P. H. Ballentine, A. M. Kadin, and D. S. Mallory, IEEE Trans. Magn. **27**, 997 (1991).

26. S. Witanachchi *et al.*, Appl. Phys. Lett. **53**, 234 (1988).

27. J. R. Gavaler *et al.*, J. Appl. Phys. **70**, 4383 (1991).

28. P. H. Ballentine, A. M. Kadin, M. A. Fisher, D. S. Mallory, and W. R. Donaldson, IEEE Trans. Magn. **25**, 950 (1989).

29. Photovoltage measurements [A. D. Semenov *et al.*, Appl. Phys. Lett. **60**, 903 (1992)] confirm that YBCO is indeed in the normal state under an optical excitation at the level used in our measurements.

2.B Increased Retention Time for Hydrogen and Other Gases by Polymer Shells Using Optically Transparent Aluminum Layers

A key difficulty in fabricating fuel capsules with polymer walls for inertial fusion is the high permeability of most polymers to the hydrogen isotopes used as fuel gases. In this article, it is shown that a thin aluminum layer can increase the retention time of a polymer shell for D_2 from several minutes to several hours, while remaining transparent enough to allow interferometric measurement of changes in gas content. Having achieved a time constant for gas retention of an hour or more, a shell can be filled with fuel gas (along with a diagnostic gas such as Ar or Ne), and the Al layer thickened before a significant amount of the gas permeates out. This thicker Al layer greatly increases the time constant, but being opaque, prevents further interferometric characterization. Because many days may elapse before the capsule is used in an inertial-fusion experiment, slow loss of fuel is prevented by storing the capsule in pressurized fuel gas until the day of use.

Polymer shells are desirable fuel capsules for inertial-fusion experiments because they are composed of elements with low atomic number.[1] Spherical shells with the necessary high degree of uniformity may be fabricated by starting with polystyrene (PS) shells made by the microencapsulation[2,3] or drop-tower method,[4] and the walls uniformly thickened with another polymer by bouncing the shells during the coating process.[5–7] Prior to this study, the only method available for increasing the time constant for gas retention that still allowed interferometric characterization was to coat the shells with a thin layer of polyvinyl alcohol (PVA) or to incorporate such a layer between two of the other polymers. While the PVA layer can greatly increase the time constant for gas retention, this property can be significantly degraded by exposure of the PVA to beta radiation from tritium decay.[8] There is no reason to expect that similar degradation would occur with Al barrier layers.

In this study, PS shells are made by the microencapsulation method, selected for wall thickness and uniformity using optical interferometry, and the walls thickened with parylene while the shells are bounced. The shells are then glued to single support stalks of small diameter (4 μm) and coated with a thin layer of Al (45 Å to 140 Å) using a dc sputter source while being rotated under the source. The shells are then permeated with D_2, or a diagnostic gas such as Ar or Ne. Since the shells are still partially transparent, the shells can be placed in an interferometer, and the change in pressure measured as a function of time. After determination of the gas-retention time constant(s) for the gas(es) to be used, the shells are permeated to the desired pressure. A time constant of one or more hours allows the shells to be removed from the permeator and coated with additional Al without significant loss of gas. A thickness of 500 Å of Al greatly increases the time constant while also serving as a "shinethrough" barrier that prevents preheat of the fuel by the leading edge of the laser pulse during inertial-fusion experiments.

The existing data on permeability of Al to hydrogen isotopes[9] indicate that no significant permeation through the Al occurs, so the gas must be passing through discontinuities in the film. The rate of permeation observed in this study is eight to nine orders of magnitude larger than would be expected if the mechanism of permeation was similar to that of bulk Al. Characterization of the Al film and its discontinuities is beyond the scope of this study, except to note that the film is highly smooth and optically reflective and adheres well to the shell. It is also to be noted that measurements of gas permeating out of these shells show the pressure decreasing exponentially with time, which is characteristic of permeation through a polymer, not a metal.[10] In addition, it is observed that the oxidation of the Al layer, as indicated by an increase in transparency with time, is sometimes accompanied by a significant increase in the observed time constant. It can be speculated that the greater volume of the oxidized layer narrows the discontinuities through which the gas passes. (Al_2O_3 with a density of 4.0 g/cm^3 has 30% more volume per Al atom than bulk Al with a density of 2.7 g/cm^3.)

For thin Al layers, i.e., those with relatively low absorbance, a scanning Fabry-Perot interferometer is used to measure the fill-gas leakage rate through the shells in real time.[11] The technique used is reminiscent of the method by which Fabry-Perot etalons are spectrally tuned by varying the pressure of the gas between the end mirrors and, therefore, the optical path length between them, as opposed to changing their separation.[12,13] For more absorbant layers, a Mach-Zehnder interferometer is used. The pressure P remaining within the inertial-fusion target after a time t is

$$P = P_o e^{-(t-t_o)/\tau} , \qquad (1)$$

where P_o is the pressure inside the microballoon at time t_o and τ is the exponential time constant. For a gas, $n_{gas}-1$ is directly proportional to the gas pressure within the approximations imposed by both classical theory for the refractive index of rarified media and the ideal-gas law, where n_{gas} is the refractive index of the gas. In addition, the phase retardation, or shift, that a wavefront undergoes upon traversing a medium, relative to vacuum, is directly proportional to $n-1$ for that material.

To interpret the interferometric measurements, the phase shift for light passing through the center of a pressurized shell with respect to light propagating externally to it is expressed as the sum of terms caused by the gas ϕ_g and the shell ϕ_s:

$$\phi = \phi_s + \phi_g \ . \tag{2}$$

The phase shift caused by gas inside the shell is given by

$$\phi_g = m\frac{2r}{\lambda}\frac{P}{P_r}\left(n_g - 1\right), \tag{3}$$

where P is the internal pressure, r is the gas radius, n_g is the gas index of refraction at some reference pressure P_r and wavelength λ, and m is the number of times the wavefronts that produce the interferogram pass through the shell. For the Mach-Zehnder interferometer $m = 1$, while for the Fabry-Perot interferometer $m = 2$. The phase shift caused by the shell is

$$\phi_s = m\ 2w\left(n_s - 1\right)/\lambda \ , \tag{4}$$

where w is the wall thickness, and n_s is the index of refraction of the shell material.

Gas pressure inside the shell causes the shell to expand slightly, stretching and thinning the wall. It will be shown later that this thinning is significant for interferometric measurements. The change in ϕ_s because of thinning is proportional to P for thin-walled shells, and may be conveniently written as

$$\Delta\phi_s = -\alpha\,\phi_g \ , \tag{5}$$

where α is a constant for a given gas and shell material, and the pressure dependence is contained in ϕ_g.

The gas pressure measured by interferometry may be expressed, combining Eqs. (1)–(5), as

$$P_{(t)} = \frac{\left[\phi - \phi_{so}\right]\lambda\ P_r}{m\ 2r\left(n_g - 1\right)\left(1-\alpha\right)} = P_o\, e^{-(t-t_o)/\tau} \ , \tag{6}$$

where ϕ_{so} is the value of ϕ_s when $P = 0$. Since monochromatic light is used in each interferometric technique, the absolute phase shift cannot be uniquely determined. The phase shift ϕ consists of an integral part and a fractional part, of which only the fractional component is measured. This fractional component decreases continuously as a function of time, whereas the integral component changes discretely as the fractional part reaches the transition from values greater than zero to those less than 1 as the gas permeates out. When Eq. (6) is fitted to interferometric measurements of ϕ as a function of time, an arbitrary integer value is added to each measurement, and this integer is reduced by 1 each time the value of ϕ makes this transition. A least-squares fit of Eq. (6) to the data generates values of τ, P_o, and ϕ_{so}.

Both the initial pressure inside the shell P_0 and the exponential time constant τ are simultaneously measured using a computer and the following method. First, a polymer shell is filled by applying the desired pressure externally to the shell and letting it soak for an appropriate period of time (generally $t > 5\tau$) at room temperature. The external pressure is released and the initial time t_0 is recorded by the data-acquisition computer. The inertial-fusion target is inserted into the scanning Fabry-Perot or Mach-Zehnder interferometer, and individual fractional phase-shift measurements are sequentially recorded along with the elapsed time. A sufficient amount of time is allowed for most of the gas to permeate out of the shell (that is, the phase shift reaches a steady-state value as a function of time), and the data acquisition is terminated. A typical plot of fractional phase shift as a function of elapsed time is shown in Fig. 52.17(a). Integral values are added to each phase-shift value to align them and produce a continuous data set, as illustrated in Fig. 52.17(b). The aligned time-dependent phase-shift values are then least-squares curve fitted to yield a plot such as the one shown in Fig. 52.18(a), and the fitting parameters P_0, τ, ϕ_{s0}, and the standard deviation of the fit are determined. (In actuality, initial guesses for P_0, τ, ϕ_{s0}, based on the pressure to which the shell was filled and the aligned phase-shift data, are supplied to the curve-fitting routine, and these are numerically adjusted to minimize the standard deviation of the fit.) The fractional phase shift caused by the empty shell ϕ_{s0} is then subtracted from each of the fitted values, and Eq. (6) is applied to each corrected phase-shift measurement to produce the plot of gas-fill pressure versus elapsed time depicted in Fig. 52.18(b).

Exponential time constants for the permeation of argon, neon, and deuterium through Al-coated polymer shells were measured using this technique. Figure 52.19 shows results from interferometric measurements taken with a polymer

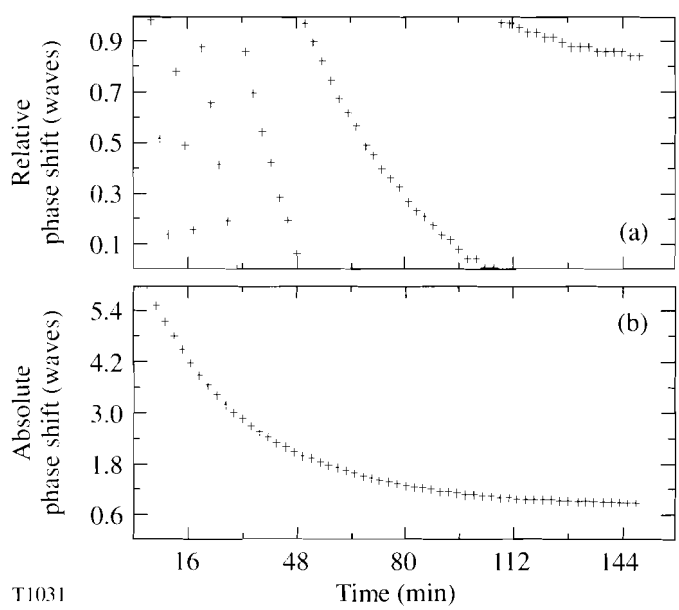

Fig. 52.17
Typical phase-shift measurements acquired using scanning Fabry-Perot interferometry. (a) The fractional phase shift imposed on light passing through an argon-filled inertial-fusion target as a function of the elapsed time since its removal from the permeation vessel. This polymer shell had a 305-μm outer diameter and consisted of a 3-μm-thick polystyrene shell overcoated with a 3-μm-thick parylene layer. The external argon pressure applied during pressurization was 21.3 atm. (b) The absolute phase shift as a function of elapsed time. Successive integers were added to adjacent groups of fractional phase shift in Fig. 52.17(a) to produce a continuous curve.

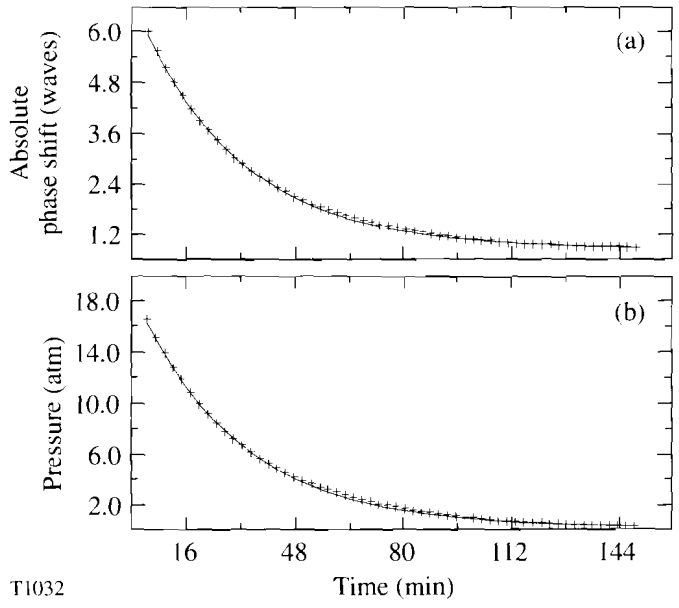

Fig. 52.18
(a) The least-squares curve fit to the absolute-phase-shift-versus-elapsed-time data given in Fig. 52.17(b). (b) The corresponding least-squares curve fit of its internal pressure versus elapsed time, which was derived from the data given in Fig. 52.17(b). The curve fit yields an initial, internal argon pressure of 19.2 atm and a 30.6-min, exponential-decay time constant.

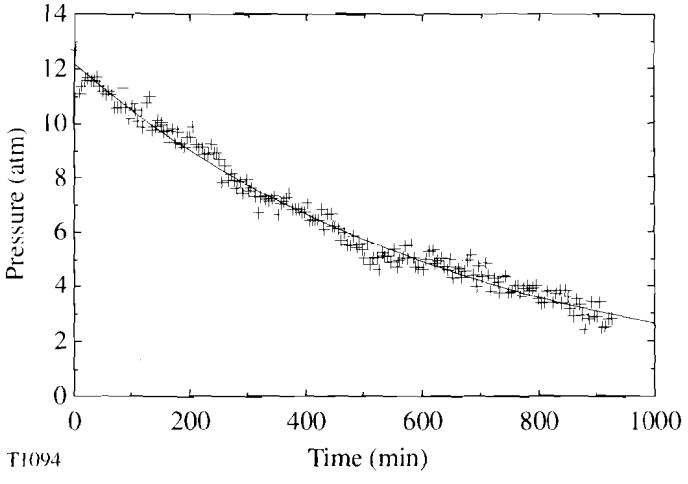

Fig. 52.19
The internal pressure of a D_2 shell as a function of time measured with Mach-Zehnder interferometry. This shell was overcoated with a 90-Å-thick Al layer, which produced a time constant of about 11 h.

shell having a 261-μm outer diameter and composed of a 3-μm-thick polystyrene shell overcoated with a 3-μm-thick parylene layer and a 90-Å-thick sputtered Al layer. It was filled by applying an external D_2 pressure of 15.0 atm at room temperature and then allowing it to soak at that pressure for 72 h. The results of the least-squares curve fit for this inertial-fusion target are an initial pressure of 12.2 atm [using $(n_{gas}-1)_{1\ atm} = (1.29\pm0.01)\times 10^{-4}$ @ $\lambda_o = 488.0$ nm and 25°C for D_2],[14] an exponential-decay time constant of 10.9 h, and a residual fractional phase shift of 0.19. The root-mean-squared (rms) deviation of an experimentally

determined phase-shift value from the fitted curve is 0.02, which corresponds to a standard deviation of λ/50. Without aluminum coatings, shells of these dimensions generally have a time constant of only several minutes for D_2.

Permeation time constants for Al-coated shells of similar dimensions and various Al coating thicknesses are given in Fig. 52.20; included are values for Ar, Ne, and D_2 for the same shells. For the thinner aluminum layers, the time constant varies only slightly between shells from the same batch that were coated simultaneously. However, as the thickness of the Al layer increases, a large shell-to-shell variation in time constant develops. This is assumed to be caused by the formation of aluminum islands on the surface of the shell during the early part of a coating run that coalesce into a continuous film as more material is deposited. The time constant of shells onto which a small amount of aluminum has been deposited is determined by the amount of uncoated surface area that remains between the islands following coating, whereas the time constant of shells that have received thicker, continuous films is defect limited: permeation takes place through regions in the film where its integrity is poor because of surface debris, oily films, stresses in the shell during permeation, etc. Since the amount and severity of defect sites on each shell from a given batch ranges widely, the measured time constants for these shells when simultaneously coated with a thicker layer of Al correspondingly varies, often by as much as ±30% from their average value.

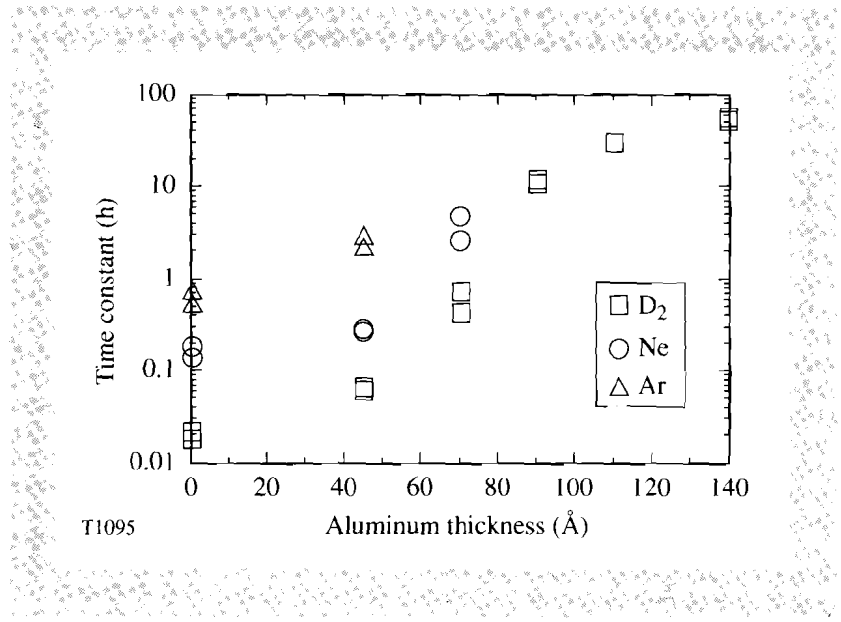

Fig. 52.20
Time constant recorded for gases permeated through shells coated with various thicknesses of Al. All targets were 250±10 μm in diameter and had 6-μm-thick polymer walls. For the 45-Å- and 70-Å-thick Al layers, the same shells were permeated and measured using D_2, Ne, and Ar.

Unlike glass shells, the initial D_2 pressure measured within polymer shells (assuming $\alpha = 0$) is consistently 10% to 20% lower than the pressure at which they were filled, whereas repeated measurements taken with the same shell are reproducible within less than one standard atmosphere. This is a real phenomenon and is not because of inadequacies of the experimental technique used to measure the fill pressure inside a microballoon. For example, in considering the possibility that air permeates back into the shells it is noted that $n_{gas}-1$ for air is about twice

the value for hydrogen at standard conditions. At most, a 2-atm discrepancy between the actual and measured initial fill pressures would occur if air did permeate into the shell during the leakage-rate measurements. Hence, considering the relatively short exponential-decay time constant measured for the hydrogen-containing shell and the comparatively large disagreement between the external pressure applied and that measured, the permeation of air into the polymer shell does not explain the initial pressure discrepancy. The most plausible explanation for this effect is stretching of the shell wall.

When the shell wall stretches because of internal gas pressure, the thinning of the wall produces a change in the original optical phase shift caused by the empty shell that is significant compared to the phase shift caused by the gas. Assuming the stretching of the shell wall is elastic, it shows up as a change in the phase shift through the center of the shell that is proportional to the internal pressure. To predict the magnitude of shell-wall thinning, consider two hemispheres being pushed apart by internal pressure. Assume that the wall thickness w is much less than the radius r, so that strain can be treated as uniform throughout the wall. In addition, treat the shell radius as identical to the gas radius. The force trying to separate the two hemispheres $\pi r^2 P$, where P is the internal pressure, acts on an annulus of area $2\pi rw$, so that the stress is $Pr/2w$. This results in a strain $\Delta r/r$ given by the ratio of stress to Young's modulus Y

$$\frac{\Delta r}{r} = \frac{Pr}{2Yw} . \tag{7}$$

The change in ϕ_s [Eq. (4)] caused by shell expansion $\Delta\phi_s$ is independent of the compressibility of the shell. This may be seen by noticing that w is proportional to $(\rho r^2)^{-1}$, where ρ is the density of the shell material. Since $n_s - 1$ is, to a good approximation, proportional to ρ, then ϕ_s is independent of ρ and is proportional to r^{-2}. Using this fact, we observe $\Delta\phi_s = -2\phi_s \Delta r/r$. Combining this with Eqs. (4) and (7),

$$\Delta\phi_s = \frac{-2mPr(n_s - 1)}{\lambda Y} . \tag{8}$$

The ratio of $\Delta\phi_s$ to ϕ_g is independent of shell dimensions and pressure and depends only on the refractive indices and Young's modulus. Note that this defines the quantity α introduced in Eq. (5):

$$\frac{\Delta\phi_s}{\phi_g} = -\frac{P_r}{Y}\frac{(n_s - 1)}{(n_g - 1)} = -\alpha . \tag{9}$$

Using typical values for polystyrene, $Y = 3200$ MPa, $n_s = 1.59$, we find for the gases D_2, He, Ne, and Ar, values of α are 0.15, 0.58, 0.30, and 0.07, respectively, at $\lambda = 546$ nm and a temperature of 25°C. These values can be used to correct the interferometric measurement of phase as a function of time as the gas permeates out of the shell. Precise agreement with these numbers is not expected because the parylene layer has different values of Y and n_s.

Inertial-fusion targets containing several gases, each with significantly different permeation time constants, have been made using aluminum gas-barrier layers. For example, various mixtures of D_2 and Ar were permeated into Al-coated polymer shells using the following procedure. The shells are first evacuated by placing them in vacuum overnight, either in the sputter coater's vacuum chamber or a separate, evacuated cell. (The time constant for air to permeate from within a shell with dimensions similar to those in Fig. 52.20 is about 1 h.) They are then coated with 45 Å of aluminum, which yields a time constant of about 2 h for Ar in a shell with a 250-μm outside diameter. The shells are then permeated to the desired partial pressure of Ar. A second Al layer is coated over the first to increase the total time constant to a value acceptable for retaining the D_2. The thickness of the second Al layer is 80 Å to 90 Å, as determined from data such as that in Fig. 52.20, and this coating is completed within a time interval that is much shorter than the Ar time constant for the first coating, typically in less than 10 min. The shell is then permeated with the appropriate gas mixture. A final 500-Å-thick Al coating that serves as a shinethrough barrier is applied in a time much less than the time constant for D_2 permeation, and the coated shell is returned to the permeation cell to soak in the gas mixture until it is loaded into the target chamber.

Although the measured time constants for shells from the same batch that were coated simultaneously often vary significantly, especially those with thicker layers of Al, out of the nearly 100 shells tested during the development of this barrier-layer technique, no shells lost gas because of an inexplicable failure of the aluminum layer. Those shells that did fail to hold gas were found to have small cracks in their walls when examined with a high-power optical microscope. We have, therefore, found optically transparent aluminum layers to be an extremely reliable technique for retaining gases within polymer shells for inertial-fusion experiments.

ACKNOWLEDGMENT

This work was supported by the U.S. Department of Energy Office of Inertial Confinement Fusion under agreement No. DE-FC03-85DP40200 and by the Laser Fusion Feasibility Project at the Laboratory for Laser Energetics, which is sponsored by the New York State Energy Research and Development Authority and the University of Rochester.

REFERENCES

1. J. Nuckolls *et al.*, Nature **239**, 139 (1992).
2. U. Kubo, M. Nakatsuka, and M. Tsubakihara, Annual Progress Report, ILE, Osaka University, ILE-APR-79 (1979), p. 177.
3. LLE Review **42**, 70 (1990).
4. A. K. Burnham, J. Z. Grens, and E. M. Lilley, J. Vac. Sci. Technol. A **5**, 3417 (1987).
5. R. Q. Gram, C. K. Immesoete, H. Kim, and L. Forsley, J. Vac. Sci. Technol. A **6**, 2998 (1988).
6. S. A. Letts, D. W. Myers, and L. A. Witt, J. Vac. Sci. Technol. **19**, 739 (1981).

7. R. Liepins *et al.*, J. Vac. Sci. Technol. **18**, 1218 (1981).

8. L. A. Scott, R. G. Schneggenburger, and P. R. Anderson, J. Vac. Sci. Technol. A **4**, 1155 (1986).

9. P. C. Souers, *Hydrogen Properties for Fusion Energy* (University of California Press, Berkeley, CA, 1986), p. 371.

10. *Ibid.*, p. 370.

11. M. D. Wittman, D. Malacara, and H.-J. Kong, in *Laser Interferometry IV: Computer-Aided Interferometry* (SPIE, Bellingham, WA, 1991), Vol. 1553, p. 456.

12. R. L. Woerner and T. J. Greytak, Rev. Sci. Instrum. **47**, 383 (1976).

13. R. Wallenstein and T. W. Hänsch, Appl. Opt. **13**, 1625 (1974).

14. *International Critical Tables of Numerical Data, Physics, Chemistry and Technology*, edited by E. W. Washburn (McGraw-Hill, New York, 1930), Vol. VII, pp. 1–12.

2.C Raman Scattering of High-Power Lasers in Air

Inertial-confinement laser fusion requires propagation of high-intensity, pulse-shaped IR and UV laser beams through long air paths. Such beams are subject to losses and decreased beam quality because of stimulated rotational Raman scattering (SRRS) in the atmosphere. With short pulses, it is necessary to use transient Raman theory to include buildup and relaxation of the medium. Imperfect beam quality can lead to intensity hot spots that change the effective threshold for Raman scattering. A detailed analysis of energy conversion and beam quality necessitates a four-dimensional (4-D) treatment of the laser pump, the Stokes beam, and the air path. The SRRS model includes laser pulse shape, medium excitation and relaxation, and spontaneous scattering as a quantum initiation of the Stokes field.

Typical irradiance levels for the OMEGA Upgrade laser system are ~2 GW/cm^2, giving a steady-state gain length of about 60 cm. Depending on the particular system configuration, an air path of between 15 m and 20 m may be required, corresponding to as much as approximately 30 gain lengths. Fortunately, the transient Raman gain may be considerably less than the steady-state gain. However, the problem is exacerbated by intensity nonuniformities in the laser beam. These hot spots are common in the near field, arising from diffraction propagation of high-frequency aberrations. Raman conversion of the laser to Stokes light is enhanced at the location of hot spots, leading to a change in the overall Raman conversion.

The Stokes radiation generated in the air path arises from spontaneous Raman scattering and is subsequently amplified by stimulated Raman scattering. The origin of spontaneous Raman scattering is a low-level random polarization of the

nitrogen molecule in the air caused by quantum fluctuations. The quantum-induced medium polarization is uncorrelated spatially, referred to as delta-correlated spatially. The laser scatters off the delta-correlated polarization sites to produce Stokes light that spreads in all directions. Only the Stokes light that is primarily in the forward direction receives appreciable stimulated amplification, so we are justified in ignoring the Stokes light scattered backward and to the sides. However, the angle of the Stokes light in the forward direction, which is amplified, is still of substantial size. The solid angle of effective stimulated amplification is determined by the area of the beam divided by square of the length, which is of the order of 0.1–0.2 msterad for the OMEGA Upgrade laser system. This wide-angle Stokes radiation does not reach the fusion target in the far field, so the Raman process is a parasitic process causing beam-to-beam power imbalance. Since the rate of Stokes generation is very strongly dependent on hot spots, it is necessary to include two-dimensional (2-D) diffraction propagation of both the laser and Stokes fields. The wide-angle Stokes light requires high sampling densities leading to the need for large arrays, which make diffraction calculations difficult. Arrays of 1024 × 1024 or larger may be required, leading to a significant computational problem.

The need to treat the transient response of the medium compounds the computational difficulties. The medium responds to the radiation with a characteristic response time of 133 ps. A typical laser pulse is about 700 ps in length. It is necessary to resolve the medium response time over the course of the pulse, leading to the requirement of several hundred time samples, each of which requires diffraction and kinetic calculations for the large arrays.

To further add to our difficulties it is necessary to represent the state of the medium (air) at many axial positions with the same array size as the typical beams. Fortunately, it is not necessary to fully resolve the 32 gain lengths with axial samples. To the extent that the governing medium equations are at least piece-wise analytically described, the axial spacing may be extended. Instead of the several hundred axial samples needed to resolve a maximum of 32 gain lengths, only about 30–40 axial samples will suffice. In order of importance, we seek to minimize the size of the arrays because of diffraction calculations, the number of medium arrays, and finally the number of time steps.

Physics of Stimulated Raman Scattering

In light of the practical difficulties imposed by the high sampling requirements, both transverse and axial, and the large temporal-sampling necessities, the numerical methods must be designed with optimum computational efficiency. To apply the Raman model to the laser-fusion application, it is necessary to incorporate the model into a comprehensive system-analysis program capable of modeling all components, aberrations, diffraction propagation, etc. The laser analysis program GLAD was chosen for this purpose. GLAD operates on a variety of computers ranging from IBM PCs to Cray supercomputers.[1]

The governing Raman equations are[2]

$$\left[\nabla_{\perp}^{2} + 2ik_L \frac{\partial}{\partial z}\right] E_L = 2k_3 k_L Q E_s, \qquad \text{laser depletion,} \tag{1}$$

$$\left[\nabla_{\perp}^2 + 2ik_S \frac{\partial}{\partial z}\right] E_S = 2k_2 k_S Q^* E_L, \quad \text{Stokes amplification, and} \tag{2}$$

$$\frac{\partial Q^*}{\partial t} = -\Gamma Q^* + ik_1 E_L^* E_S + F^*, \quad \text{medium nonlinear polarization,} \tag{3}$$

where E_L and E_S are the laser and Stokes complex amplitudes and Q is the medium polarization. The respective wave numbers are k_L and k_S. The gain medium constants are k_1, k_2, and k_3. Γ is the Raman bandwidth and F is a delta-correlated random force representing random dephasing caused by collisions. Equations (1) and (2) define the diffraction propagation and the effect of the medium polarization Q on the optical fields E_L and E_S. Equations (1) and (2) are expressed in a coordinate system moving at the speed of light. Equation (3) defines the temporal behavior of the medium polarization in terms of the product of the optical fields and the random collisional force F. Solution of these three equations has been extensively explored in the literature under various approximations. References 2, 3, and 4 are representative. References 5 and 6 describe some of the interesting experiments that have been conducted.

The form of the exact solution, including diffraction, but neglecting pump depletion, invokes a three-dimensional convolution in space and a convolution in time. While the solution is elegant, the spatial and temporal convolutions are very difficult to implement for the numerous large arrays needed to describe the optical fields and the medium polarization. This solution has been most readily applied to very low Fresnel-number problems. In our application, Fresnel numbers of about 10,000 are typical and the difficulties of direct Green's-function solutions are more serious.

We elected to develop our model from the basic differential equations. We may separate the diffraction and the optical-field interactions with the medium using the split-step method.[7,8] This allows FFT methods to be used for diffraction propagation.

$$\frac{\partial E_L}{\partial z} = \frac{i}{2k_L} \nabla_{\perp}^2 E_L \tag{4}$$

represents diffraction for E_L, and

$$\frac{\partial E_S}{\partial z} = \frac{i}{2k_S} \nabla_{\perp}^2 E_S \tag{5}$$

represents diffraction for E_S. The medium polarization is influenced by stimulated Raman in the form of the product of the optical fields, the collisional force, and dephasing decay associated with collisions. Since Eq. (3) indicates a linear response of Q to the two driving forces, we may treat these separately.

$$\frac{\partial Q^*_{SRS}}{\partial t} = -\Gamma Q^*_{SRS} + ik_1 E^*_L E_S(z) \tag{6}$$

represents stimulated Raman amplification and decay, and

$$\frac{\partial Q^*_{SR}}{\partial t} = -\Gamma Q^*_{SR} + F^* \tag{7}$$

represents collision effects and decay. The collisional force F of Eq. (7) forms a random-scattering field, as shown in Fig. 52.21. The variance of random component Q_{SR} is constant, although the amplitude and phase at each point varies at the Raman response time. The spontaneous Raman scattering may be modeled as a mechanism for scattering the laser pump into the Stokes field according to a constant g_2. Spontaneous Raman scatters into all directions but we consider only the radiation scattered into the forward direction as defined by $\Delta\Omega$.

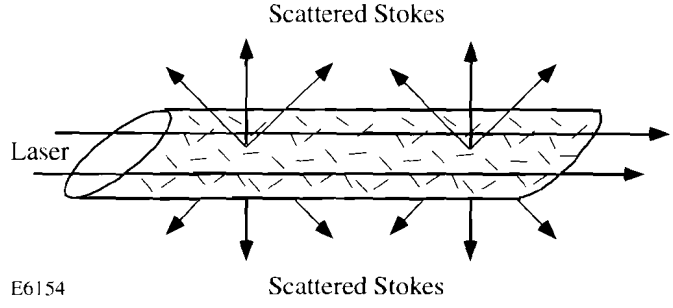

Fig. 52.21
A laser beam incident from the left is scattered by the medium field QSR, which is delta correlated spatially and scatters light into 4π steradians. Only the light scattered in the forward direction contributes to the amplified Stokes.

The random element of spontaneous Raman is treated by a set of time-evolving random phasors at each point. The spontaneous emission noise takes the form

$$\left\langle I_S(x,y,z,+\Delta z,t_n)\right\rangle = \left\langle I_S(x,y,z,t_n)\right\rangle + g_2 I_L(t_n)\frac{\lambda^2}{4\pi\Delta x\Delta y}\Delta z\ , \tag{8}$$

where g_2 is the spontaneous Raman-gain coefficient and can be determined by theoretical or experimental spontaneous Raman-scattering data, and I_L and I_S are the laser and Stokes irradiances. The factor $\Delta\Omega = \lambda^2/\Delta x\Delta y$ is the maximum solid angle represented by a computer array with sampling intervals Δx and Δy.[9] This becomes of major importance when an angle of 10 mrad may need to be represented. This leads to very fine sampling densities and necessarily very large arrays. The effect of hot spots and extremely high amplification ameliorate this effect, to some degree making the effective Stokes source much narrower.

The random noise is introduced by the use of a spatially uncorrelated random variable X, which is a unit variance complex random number, normally distributed in amplitude and uniformly distributed in phase, represented by

$$E_S(x, y, z + \Delta z, t_n) = E_S(x, y, z, t_n)$$

$$+\left[g_2 I_L(x, y, z, t_n)\frac{\Delta\Omega}{4\pi}\Delta z\right]^{1/2} X(x, y, z, t_n). \quad (9)$$

To include the finite temporal correlation, we update the random number with a second random number Y

$$X(x, y, z, t_n) = X(x, y, z, t_{n-1})e^{-\Gamma\Delta t} + Y(x, y, z, t_n)\left(1 - e^{-2\Gamma\Delta t}\right)^{1/2}. \quad (10)$$

Having considered diffraction and spontaneous Raman scattering by means of separate split-step operations, we need only add the stimulated Raman amplification

$$\frac{\partial E_L}{\partial z} = ik_3 Q E_S\ , \quad (11)$$

$$\frac{\partial E_S}{\partial z} = -ik_2 Q^* E_L\ , \quad (12)$$

$$\frac{\partial Q^*_{SRS}}{\partial t} = -\Gamma Q^*_{SRS} + ik_1 E_L^* E_S(z)\ . \quad (13)$$

Carmen *et al.*[4] give a closed-form expression for stimulated Raman amplification (ignoring pump depletion and diffraction)

$$E_S(z,t) = E_S(0,t) + (k_1 k_2 z)^{1/2} E_L(t) \int_{-\infty}^{t} e^{-\Gamma(t-t')}$$

$$\left\{E_L^*(t')E_S(0,t')\left[\tau(t) - \tau(t')\right]^{-1/2} I_1\left(2\left\{k_1 k_2 z\left[\tau(t) - \tau(t')\right]\right\}^{1/2}\right)\right\} dt'\ , \quad (14)$$

where

$$\tau(t) = \int_{-\infty}^{t} \left|E_L(t')\right|^2 dt'\ . \quad (15)$$

This approach requires that we save the temporal functions $E_L^*(t')E_S(0,t')$ and $\tau(t)$ over several response times for each transverse point and for each axial sample. If we neglect diffraction, then one axial point suffices. However, to treat the diffraction-induced hot spots, we need to have axial samples every 0.5 m to 2 m. Hence, Eq. (14) leads to the need to manipulate a very large amount of data.

Since we need a reasonable number of axial samples, we may simply solve Eqs. (12) and (13) directly. We store the time-integrated value Q*;

$$Q^*_{SRS}(z,t) = ik_1 \int_{-\infty}^{t} e^{-\Gamma(t-t')} E^*_L(z,t') E_S(z,t') dt' . \quad (16)$$

Because of the particular form of $e^{-\Gamma(t-t')}$, we do not have to save the time history of the product of $E^*_L(z,t')E_S(z,t')$ and can save only $Q^*_{SRS}(z,t)$ according to the evolving sum

$$Q^*_{SRS}(z,t+\Delta t) = Q^*_{SRS}(z,t)e^{-\Gamma\Delta t} + ik_1 e^{-\Gamma\Delta t} E^*_L(z,t)E_S(z,t), \quad (17)$$

where Δt is the temporal sampling.

We now integrate Eq. (12) through the axial samples to find E_S, including diffraction, apertures, atmospheric aberration, and any other effects that exist between the axial samples. $Q^*_{SRS}(z,t)$ varies rapidly with z, following a nearly exponential form. We make use of this nearly exponential property to reduce the number of axial samples required (see Fig. 52.22).

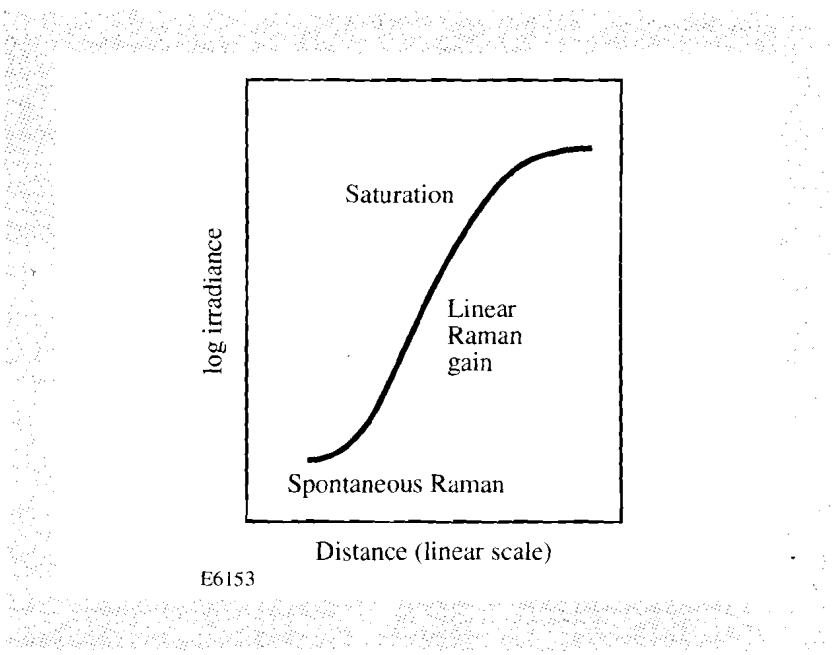

Fig. 52.22
Semi-exponential growth of Stokes light in the spontaneous regime (shown schematically).

Equation (14) and our revised methods based on Eqs. (12) and (17) give essentially identical results. It is easier to see the variation of gain with distance from Eq. (14). In the transient regime, Eq. (14) shows a square-root dependence on distance.

The beam is characterized by Fresnel numbers of the order of 10,000. This implies that diffraction effects caused by the aperture are localized to the immediate vicinity of the aperture edge and may safely be neglected. The

aberration of the laser pump may have features as small as 1 cm or less. This aberration is relatively easy to resolve using an array of 128 × 128 or larger. This type of aberration is the source of hot spots because of diffraction effects, but a centimeter-sized aberration structure forms strong hot spots over a distance of about 100 m or more but weaker hot spots over the 20-m beam path. However, diffraction in the upstream beam at smaller diameter can form hot spots over short distances, typical of a master oscillator power amplifer (MOPA) laser configuration.

The Stokes beam is characterized by very fine structure speckle. In the regime of no significant pump depletion, the amplification is linear. While spontaneous Raman light occurs throughout the entire beam path, the noise that is generated furthest upstream receives the most amplification and dominates the process. When viewed from the end of the beam path looking backward toward the start of the beam path (not recommended in practice for gigawatt beams) we would see a self-luminous fog of Stokes noise with the most upstream fog being brightest. One may consider the noise source to occur in the first gain length. The Stokes source is a delta-correlated coherent object and creates a speckle pattern with characteristic feature size of λ/θ, where θ is the subtense of the Stokes noise source as viewed by final Stokes field. The speckle size increases with beam path length but at 10 m the size is approximately 23 μm, which is too small to be resolved. However, this speckle size assumes a perfectly uniform laser pump. In actuality, the laser will inevitably have some degree of nonuniformity of irradiance.

OMEGA Upgrade Laser System

The OMEGA Upgrade laser project involves the enhancement of the existing OMEGA Nd:glass laser system for exploration of the ignition-scaling regime of inertial-confinement fusion (ICF) physics research. This project will result in a 30-kJ, 351-nm, 60-beam, direct-drive laser facility that features versatile pulse shaping using beam co-propagation and uniform target irradiation using broad-band phase-conversion techniques. The schematic illustration in Fig. 52.23 shows the relationship between beam co-propagation and the continuous pulse shapes envisioned for the OMEGA Upgrade laser system.

The final infrared energy, produced by a series of rod and disk Nd:glass amplifiers arranged in a MOPA configuration, is frequency converted to the UV and then transported to the target chamber. The path length in air is minimized with a two-mirror-per-beamline configuration (Fig. 52.24) to reduce the distance

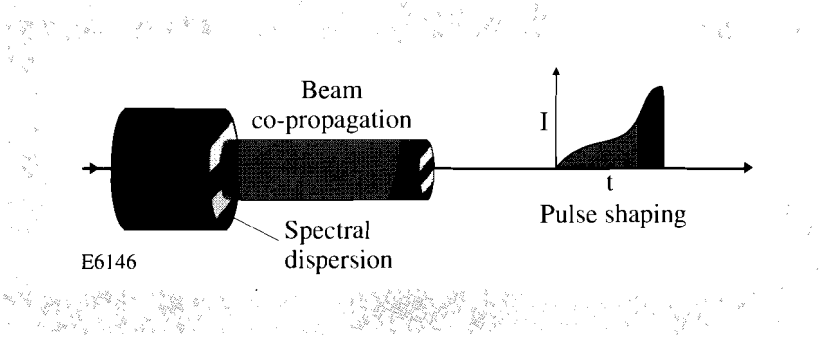

Fig. 52.23
The individual (inner and outer) portions of the co-propagated beam are electro-optically shaped to form the continuous pulse shape used in the OMEGA Upgrade laser system.

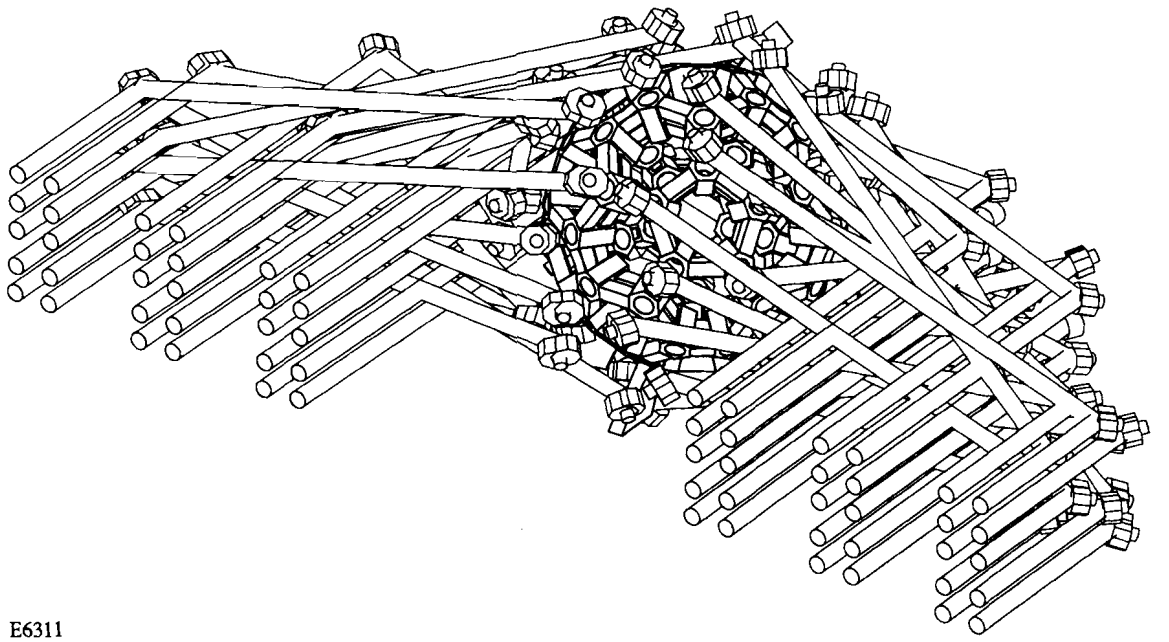

E6311

Fig. 52.24
The OMEGA Upgrade laser system includes an ultraviolet transport system that requires an 18-m path in air between the frequency-conversion cell and the final focus lens.

over which an intense beam propagates in a nitrogen-rich environment. Considerations of conversion efficiency, on-target energy balance, and system flexibility resulted in a propagation distance of ≤20 m between frequency-conversion cells and the focusing lens of the target chamber. Although preliminary estimates of SRRS efficiency showed that operation of the OMEGA Upgrade laser at full design energy remained below threshold for SRRS, further investigation of near-threshold operation is an important consideration for meeting performance requirements over the entire life of the laser.

The parameters used within this GLAD SRRS code are contained in Table 52.III. The peak laser-beam irradiance listed is consistent with the 30-kJ, full-system UV output. The gIL product, assuming steady-state gain, is approximately 25, which indicates near-threshold condition. However, the Gaussian and continuous pulse-shaped temporal profiles envisioned for use on the laser are short enough that below-threshold operation of the laser is predicted. Figures 52.25 and 52.26 illustrate the transient response to the baseline Gaussian and pulse-shaped temporal waveforms of the laser pump, respectively. The resulting Stokes temporal waveform follows the peak of the laser by about one Raman time constant as can be seen as a temporal delay between peaks in Fig. 52.25.

An increase in the Stokes radiation occurs for the actual shaped pulses planned for the OMEGA Upgrade laser. Using the parameters listed in Table

52.III, except for the duration over which the peak fluence occurs based on the pulse shape, a slightly greater amount of Stokes light is produced as would be expected. Although this does not present a problem, operation of the laser near threshold warrants closer examination of the detailed conditions regarding pulse-shaping, angular dispersion, and beam profile.

Table 52. III: Parameters used in transient Raman calculations.

Beam diameter	28 cm
Propagation length	18 m
Fresnel number	$\sim 10^4$
gIL product (steady-state)	~25
Laser wavelength	0.3511 μ
Stokes wavelength	0.35203 μ
Peak laser irradiance	2×10^9 W/cm^2
Initial Stokes irradiance	0
Laser pulse width	700 ps FWHM (Gaussian) and pulse shaped
Raman bandwidth	7.52×10^9 sec^{-1}
Stimulated Raman steady-state gain g_1	6.76×10^{-12} cm/W
Spontaneous Raman gain g_2	6.416×10^{-9} cm^{-1}

E6339

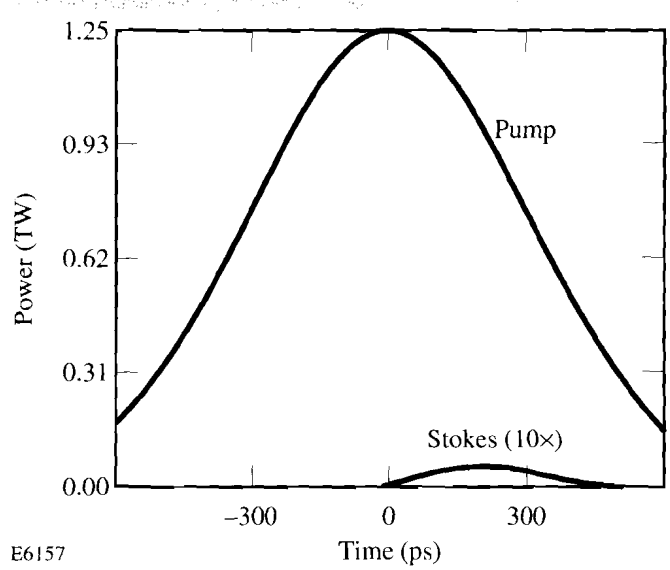

Fig. 52.25
A Gaussian temporal waveform for the laser input produces a Stokes pulse that is delayed according to the SRRS response time. These results indicate that the OMEGA Upgrade laser can operate at full beam fluence while remaining below SRRS threshold.

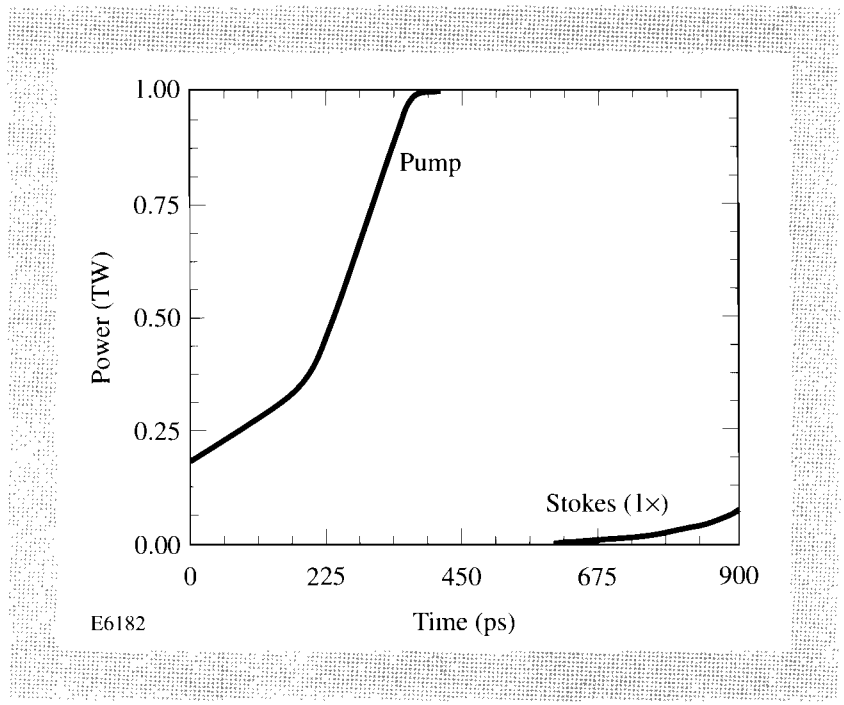

Fig. 52.26
Raman conversion of a shaped pulse is somewhat larger than that for a Gaussian pulse because of the longer time interval at peak beam irradiance.

Experimental Investigations

Previous experimental investigations[5,6,10] of Raman scattering in air involved either excessively long air paths with small beam diameters or poor beam quality, both of which make 4-D theoretical comparisons difficult, if not impossible. Poor beam quality can give rise to severe intensity variations in the near field of a beam leading to nonuniform Stokes production as well as high Stokes irradiances, which can cause premature growth of the secondary Stokes radiation. Experiments conducted under these conditions do not necessarily provide results that can be scaled to shorter paths with higher pump irradiance, such as the beamlines of the OMEGA Upgrade. In addition, aberrated pump beams often give rise to large statistical variations of the measured Raman conversion efficiency, presumably because of a greater sensitivity to gain variation for the various random noise fields.

The experimental setup, schematically illustrated in Fig. 52.27, is used to investigate Raman scattering in air within the OMEGA laser facility. The output of the 90-mm rod amplifier is directed to the prototype beamline consisting of the 15- and 20-cm SSA amplifiers, each followed by a vacuum spatial filter. Infrared laser beams, with energies between 100 J and 400 J, a beam diameter of 18 cm, and a 700-ps to 750-ps (FWHM) pulse width, are frequency converted to produce between 50 J to 150 J of UV ($\lambda = 351$-nm) laser light. The frequency-tripled light is characterized with near-field photography and calorimetry. The UV beam is transported along an air path of 45 m and directed to a diagnostic station consisting of a near-field camera, a one-dimensional (1-D) spectrometer, and a 2-D imaging spectrometer. The light propagated to the 1-D spectrometer is phase converted with a UV distributed phase plate (DPP) to provide uniform sampling of the near field at the slit of the spectrometer without creating high irradiance, which can cause scattering mechanisms within the diagnostic itself.

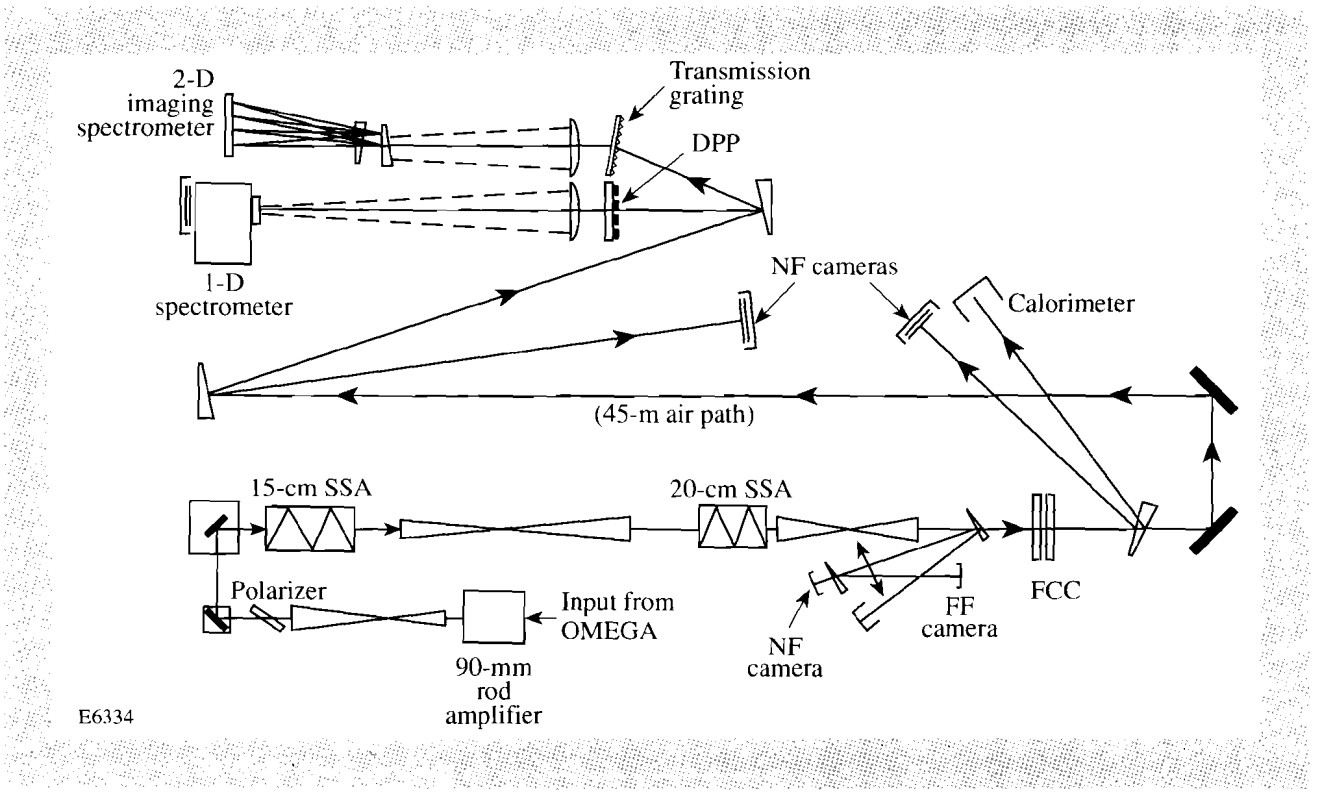

Fig. 52.27
The experimental layout used to study SRRS in air consisted of a frequency-tripled SSA beamline and several laser-beam diagnostics. The diagnostics included near-field photography and calorimetry, as well as 1-D and 2-D far-field spectroscopy using diffractive optics. The 1-D grating spectrometer possessed four to five orders of magnitude in dynamic range to cover a gIL range of between 15 and 40.

The 2-D spectrometer is constructed with a UV transmission grating (1800 grooves/mm) followed by a 5-m lens, which together provides a 1-cm/nm separation of the 2-D pump and Stokes beams. The beam profile and spectra are all recorded on Kodak 4421 Aerographic film.

The results of converting a UV laser pump to Stokes light, over a (gIL) product range of 5–40, are shown in Fig. 52.28. The solid theoretical curve is generated from the SRRS code using the measured intensity distribution at the input to the Raman air path. This takes into account the actual intensity nonuniformities, but does not include the cumulative phase-front errors caused by the multi-element optical system producing the infrared laser beam. The dominant nonuniformity is a slowly varying edge-peaked profile.

An excellent agreement between the theoretical predictions and experimental results is shown in Fig. 52.28. The error bars for the two highest values for Raman conversion are large because of a vignetting of the Stokes beam prior to it reaching the slit of the spectrometer. A uniform Stokes beam, consisting of fine speckle, is expanded to a near-field beam diameter greater than that of the laser pump for gIL values greater than 35. The dynamic range of the 1-D spectrometer covers four to five orders of magnitude, making it possible to accurately compare

the experimental results to theoretical predictions, both well below and well above SRRS threshold. For gIL values of 5 A to 15 A, zero value for the Stokes light was recorded, placing an upper bound on the measurement. Reproducibility of this upper-bound measurement, together with six data points representing gIL products of between 25 and 40, provides excellent confidence in the theoretical modeling. These results indicate that it is possible to use detailed diffraction analysis to investigate the dependence that Raman conversion has on variations in pulse shape and beam profile.

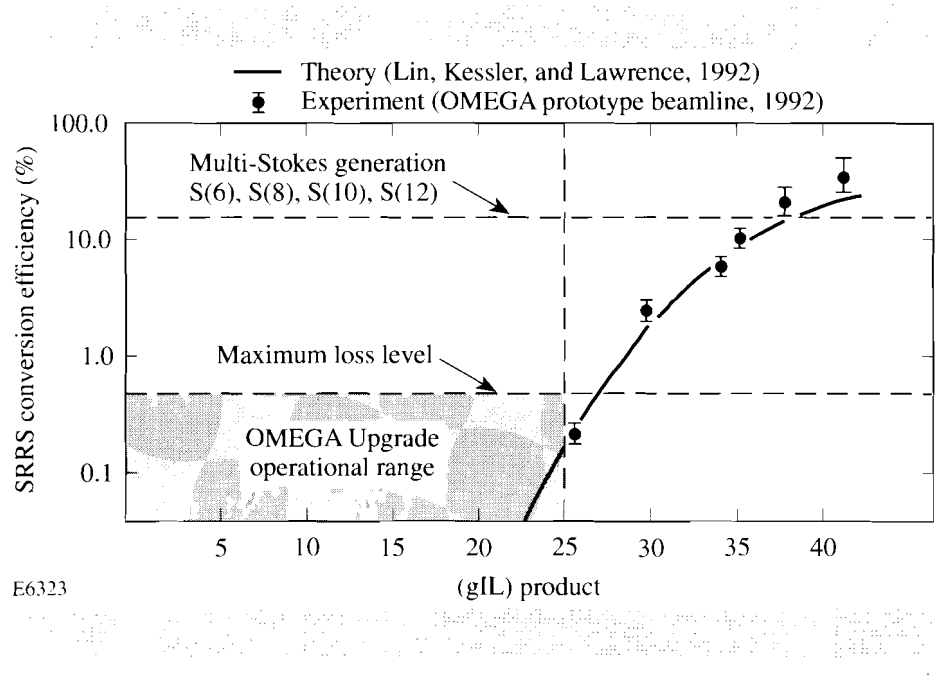

Fig. 52.28
The experimental results for Raman conversion are in excellent agreement with the 4-D SRRS code developed within GLAD. The OMEGA Upgrade laser system is designed with an ultraviolet propagation path short enough to limit SRRS conversion to less than 1/2% of the total energy. Specific limits of beam profile and temporal pulse shape can be determined by use of the new SRRS code.

These experimental results also show a Stokes production that is significantly different than that of previous investigations. The S(8) and S(10) Stokes, $\lambda = 9.39$ Å and 11.38 Å, respectively, are observed first, are nearly equal in strength, and dominate all other Stokes well past the 1% threshold. Above 10% Raman conversion the S(6) and S(12) Stokes, $\lambda = 7.41$ Å and 13.36 Å, respectively, appear; however, they remain below the S(8) and S(10) Stokes up to a gIL product of 40, which is approximately where 50% of the laser pump converts to Raman light. Previous experiments had shown secondary Stokes, antiStokes, and other molecular transitions. It is likely that beam nonuniformities present in the pump beam, for previous experiments, caused high-irradiance Stokes light. High irradiances caused by nonuniform pump and strong spatial correlation of the Stokes lead to gIL products that exceed secondary threshold. It appears that good beam quality leads to uniformly distributed Raman speckle and less complicated Stokes production mechanisms.

Both the theoretical predictions and experimental results indicate that the beamline of the OMEGA Upgrade laser system will generate low levels of SRRS over its nominal operating conditions.

Summary and Conclusion

A 4-D model of the effects of transient Raman scattering in the atmosphere has been incorporated into a general laser-system code. The model includes spontaneous and stimulated Raman scattering and accurately treats diffraction propagation and general laser intensity and phase distributions. The results presented here are preliminary and considerable work remains to characterize the OMEGA Upgrade laser system over an extended range of operating conditions. However, both theoretical and experimental results indicate that the level of Raman conversion in air will be acceptable over the full range of operating conditions. Further studies will seek to determine the limits of system energy, pulse width, and beam quality.

ACKNOWLEDGMENT

This work was supported by the U.S. Department of Energy Office of Inertial Confinement Fusion under agreement No. DE-FC03-85DP40200 and by the Laser Fusion Feasibility Project at the Laboratory for Laser Energetics, which is sponsored by the New York State Energy Research and Development Authority and the University of Rochester.

REFERENCES

1. GLAD is a proprietary product of Applied Optics Research, Tucson, AZ.
2. M. G. Raymer and J. Mostowski, Phys. Rev. A **24**, 1980 (1981).
3. C.-S. Wang, Phys. Rev. **182**, 482 (1969).
4. R. L. Carmen *et al.*, Phys Rev. A **2**, 60 (1970).
5. M. A. Henesian, C. D. Swift, and J. R. Murray, Opt. Lett. **10**, 565 (1985).
6. M. D. Skeldon and R. Bahr, Opt. Lett. **16**, 366 (1991).
7. R. H. Hardin and F. D. Tappert, SIAM Rev. **15**, 423 (1973).
8. G. N. Lawrence, "Optical Modeling," in *Applied Optics and Optical Engineering XI*, edited by R. R. Shannon and J. C. Wyant (Academic Press, New York, 1992), pp. 125–200.
9. M. D. Feit and J. A. Fleck, Jr., J. Opt. Soc. Am. B **7**, 2048 (1990).
10. N. A. Kurnit *et al.*, "Raman Scattering of Variable-Bandwidth KrF Laser Radiation in Long Air Paths," in *Conference on Lasers and Electro-Optics 1992 Technical Digest Series, Volume 12*, Anaheim, CA, 10–15 May 1992, paper CFA3.

Section 3
NATIONAL LASER USERS FACILITY NEWS

Scientists from the Naval Research Laboratory (NRL), Plasma Physics Research Institute, University of Florida, and University of Syracuse visited the laboratory during the fourth quarter of FY92. Their primary activity was to plan target shots for FY93. **A. Honig** from the University of Syracuse and **K. Mizuno** from the Plasma Physics Research Institute also did preliminary target shots. The planned experiments need to be coordinated with the LLE experimental program during the next quarter since the OMEGA laser-system upgrade will begin 18 December 1992.

J. Seely from NRL visited to discuss the high-resolution spectrograph they are building for the spectroscopy experiments to be conducted during the first quarter of FY93. **P. Jaanimagi** and **B. Yaakobi** from LLE participated in the initial design of this instrument: a flat-crystal spectrograph coupled to a streak camera able to record the time dependence of the x-ray line shapes. Diagnostic gases are to be added to the D_2 fuel, and x-ray emission from these gases will be used to characterize the target implosion.

K. Mizuno tested the Thomson scattering detector that will be used for the experiments proposed by **J. DeGroot** of the University of California at Davis. This diagnostic is designed to measure the properties of the plasma near the critical surface (where the plasma frequency equals the laser frequency). The detector was tested during a series of long-scale-length plasma experiments conducted by **W. Seka** of LLE.

C. Hooper from the University of Florida visited to discuss the argon spectroscopy experiments planned for the next quarter. He plans to use the spectrograph being built by NRL, which will allow him to measure the line shapes of the argon emission more accurately than in his previous experiments. These data will be compared with the calculations being done at the University of Florida, and the comparison will be used to characterize the conditions of the imploded core.

A. Honig transported the first of his cryogenic targets from Syracuse to be shot on the OMEGA laser. The first shot was to be on a target delivered frozen to the target-chamber center and then allowed to warm to a gaseous state before the laser irradiation. This was done to try to establish that a target could be delivered cold to the target-chamber center, and then the yield from the gaseous target could be used to establish a baseline for subsequent target shots. The experiment was not completed.

ACKNOWLEDGMENT

This work was supported by the U.S. Department of Energy Office of Inertial Confinement Fusion under agreement No. DE-FC03-85DP40200.

Section 4
LASER SYSTEM REPORT

4.A GDL Facility Report

The refurbishment of the GDL laser facility, coordinated by **J. Kelly**, began during the fourth quarter of FY92 and is expected to be completed in late FY93.

The laser room, control room, and experimental target room are being modernized, and space has been made in the laser room to accommodate the 15-cm and 20-cm disk amplifiers currently being tested on the OMEGA laser.

The current OMEGA target chamber and its attendant diagnostics will serve as the new GDL target chamber and will be available to future GDL experimenters.

4.B OMEGA Facility Report

The OMEGA system fired 531 shots during the fourth quarter of FY92, including shots used for laser testing, long-scale-length plasma experiments, damage testing of coatings for the OMEGA Upgrade, stimulated rotational Raman scattering (SRRS) experiments, and the installation of a new pulse shaper in the OMEGA driver line. The new pulse shaper will be used for a series of target experiments studying the effect of fast-rising pulse shapes on implosions of both glass and CH targets.

Four primary experimental programs were conducted simultaneously during these shots. The testing of the 15-cm and 20-cm disk amplifiers used one of the 24 beamlines, damage testing of large optics used a second beamline, the remaining beamlines were used for long-scale-length plasma experiments, and SRRS experiments used the output of the 15-cm and 20-cm amplifiers when it was available. After the completion of these experiments, the new pulse-shaper installation was started in the driver line.

The shot summary for the OMEGA laser this quarter is as follows:

Driver line	173
Laser development	117
Target	211
Software test	30
TOTAL	531

ACKNOWLEDGMENT

This work was supported by the U.S. Department of Energy Office of Inertial Confinement Fusion under agreement No. DE-FC03-85DP40200 and by the Laser Fusion Feasibility Project at the Laboratory for Laser Energetics, which is sponsored by the New York State Energy Research and Development Authority and the University of Rochester.

PUBLICATIONS AND CONFERENCE PRESENTATIONS

Publications

E. M. Epperlein and R. W. Short, "Nonlocal Heat Transport Effects on the Filamentation of Light in Plasmas," Phys. Fluids B **4**, 2211 (1992).

E. M. Epperlein, R. W. Short, and A. Simon, "Damping of Ion-Acoustic Waves in the Presence of Electron-Ion Collisions," Phys. Rev. Lett. **69**, 1765 (1992).

M. J. Guardalben and N. George, "Speckle Observation of Pulsed Laser-Induced Dynamics in a Guest-Host, Smectic-A Liquid Crystal System," Liq. Cryst. **12**, 689 (1992).

J. W. Herman and H. E. Elsayed-Ali, "Superheating of Pb(111)," Phys. Rev. Lett. **69**, 1228 (1992).

S. Krishamurthy and S.-H. Chen, "A Comparative Study of Helical Sense and Twisting Power in Low Molar Mass and Polymeric Chiral Nematics," Macromolecules **25**, 4489 (1992).

S. Krishnamurthy, S.-H. Chen, and T. N. Blanton, "Mesomorphic Behavior of Side-Chain Copolymers Containing Chiral as Well as Nematogenic Moieties Comprising *p*-Phenylene and *trans*-Cyclohexylene Rings," Macromolecules **25**, 5119 (1992).

G. G. Luther and C. J. McKinstrie, "Transverse Modulational Instability of Counterpropagating Light Waves," J. Opt. Soc. Am. B **9**, 1047 (1992).

R. S. Marjoribanks, M. C. Richardson, P. A. Jaanimagi, and R. Epstein, "Electron Temperature Measurement in Laser-Produced Plasmas by the Ratio of Isoelectronic Line Intensities," Phys. Rev. A **46**, 1747 (1992).

C. J. McKinstrie and R. Bingham, "Stimulated Raman Forward Scattering and the Relativistic Modulational Instability of Light Waves in Rarefied Plasma," Phys. Fluids B **4**, 2626 (1992).

J. Peatross, M. V. Fedorov, and D. D. Meyerhofer, "Laser Temporal and Spatial Effects on Ionization Suppression," J. Opt. Soc. Am. B **9**, 1234 (1992).

W. Seka, R. E. Bahr, R. W. Short, A. Simon, R. S. Craxton, D. L. Montgomery, and A. E. Rubenchik, "Nonlinear Laser-Matter Interaction Processes in Long-Scale-Length Plasmas," Phys. Fluids B **4**, 2232 (1992).

L. J. Shaw-Klein, S. D. Jacobs, S. J. Burns, and J. C. Lambropoulos, "Microstructural Control of Thin-Film Thermal Conductivity," in *Laser-Induced Damage in Optical Materials: 1991* (SPIE, Bellingham, WA, 1991), Vol. 1624, pp. 346–361.

L. J. Shaw-Klein, T. K. Hatwar, S. J. Burns, S. D. Jacobs, and J. C. Lambropoulos, "Thermal Conductivity of Amorphous Rare Earth–Transition Metal Thin Films for Magneto-Optic Recording," Thin Solid Films **216**, 181 (1992).

M. M. Tedrow, J. H. Kelly, M. J. Shoup III, R. Juhala, A. Reynolds, L. Allen, and G. Dubé, "Characterization of a Diode-Pumped, 3.8-cm Clear Aperture, High-Gain, Active-Mirror Laser Amplifier Using CR:Nd:GSGG and Nd:GGG," in *OSA Proceedings on Advanced Solid State Lasers*, edited by L. L. Chase and A. A. Pinto (OSA, Washington, DC, 1992), Vol. 13, pp. 223–226.

Forthcoming Publications

S. Alexandrou, R. Sobolewski, and T. Y. Hsiang, "Time-Domain Characterization of Bent Coplanar Waveguides," to be published in the *IEEE Journal of Quantum Electronics*.

S. Alexandrou, R. Sobolewski, C.-C. Wang, and T. Y. Hsiang, "Subpicosecond Electrical Pulse Generation in GaAs by Nonuniform Illumination of Series and Parallel Transmission Line Gaps," to be published in the *Proceedings of Ultrafast Electronics & Optoelectronics*, San Francisco, CA, 25–27 January 1993.

J. J. Armstrong and T. J. Kessler, "Holographic Generation of Ultra-High-Efficiency Large-Aperture Transmission Diffraction Gratings," to be published in the *Proceedings of SPIE's 1992 International Symposium on Optical Applied Science and Engineering*, San Diego, CA, 19–24 July 1992.

C. Bamber, W. R. Donaldson, E. Lincke, and A. C. Melissinos, "Electron Acceleration Using Laser-Driven Photoconductive Switching," to be published in *Nuclear Instruments & Methods A*.

C. Bamber, W. R. Donaldson, E. Lincke, and A. C. Melissinos, "A Pulsed-Power Electron Accelerator Using Laser-Driven Photoconductive Switches," to be published in the *Proceedings of the Third Advanced Accelerator Concepts Workshop*, Port Jefferson, NY, 15–19 June 1992.

D. K. Bradley, P. M. Bell, J. D. Kilkenny, R. Hanks, O. Landen, P. W. McKenty, P. A. Jaanimagi, and C. P. Verdon, "High-Speed Gated X-Ray Imaging for ICF Target Experiments," to be published in the *Review of Scientific Instruments*.

X. D. Cao and C. J. McKinstrie, "Solitary-Wave Stability in Birefringent Optical Fibers," to be published in the *Journal of the Optical Society of America B.*

S. Y. Chou, Y. Liu, W. Khalil, M. I. Nathan, T. Y. Hsiang, and S. Alexandrou, "Ultrafast Nanoscale Metal-Semiconductor-Metal Photodetectors on Bulk and Low-Temperature-Grown GaAs," to be published in *Applied Physics Letters.*

Y.-H. Chuang, L. Zheng, and D. D. Meyerhofer, "Propagation of Light Pulses in a Chirped-Pulse-Amplification Laser," to be published in *IEEE Journal of Quantum Electronics.*

A. Denysenko, S. Alexandrou, C.-C. Wang, R. Sobolewski, T. Hsiang, W. R. Donaldson, and D. K. Bradley, "Dielectric Determination of a Microstrip Channel Plate by Picosecond Electro-Optic Sampling," to be published in the *Proceedings of Ultrafast Electronics & Optoelectronics*, San Francisco, CA, 25–27 January 1993.

W. R. Donaldson and A. C. Melissinos, "A Novel High Brilliance Electron Source," to be published in the *Proceedings of the Third Advanced Acceleration Concepts Workshop*, Port Jefferson, NY, 15–19 June 1992.

W. R. Donaldson and L. Mu, "The Effects of Doping on Photoconductive Switches as Determined by Electro-Optic Imaging," to be published in the *Proceedings of SPIE's OE/LASE*, Los Angeles, CA, 20–25 January 1992.

H. E. Elsayed-Ali and T. Juhasz, "Femtosecond Time-Resolved Thermomodulation of Thin Gold Films with Different Crystal Structures," to be published in *Physical Review B.*

E. M. Epperlein, "Laser Filamentation in Plasmas," to be published in the *Proceedings of the Topical Conference on Research Trends in Inertial Confinement Fusion*, La Jolla, CA, 4–6 February 1991.

E. M. Epperlein and R. W. Short, "Comment on 'Modification of Stimulated Brillouin, Saturated Raman Scattering and Strong Langmuir Turbulence by Nonlocal Heat Transport,' " to be published in *Physics of Fluids B.*

P. M. Fauchet, D. Hulin, A. Mourchid, and R. Vanderhaghen, "Ultrafast Thermal Nonlinearities in Amorphous Silicon," to be published in *Ultrafast Laser Probe Phenomena in Semiconductors and Superconductors.*

P. M. Fauchet, "Picosecond Spectroscopy in Solids with a Free-Electron Laser," to be published in *Spectroscopic Characterization Techniques for Semiconductor Technology IV* (invited paper).

P. M. Fauchet and T. Gong, "Femtosecond Dynamics of Hot Carriers in GaAs," to be published in the *Proceedings of SPIE's 1992 Symposium on Compound Semiconductor Physics and Devices*, Somerset, NJ, 22–26 March 1992 (invited paper).

T. Gong, K. B. Ucer, L. X. Zheng, G. W. Wicks, J. F. Young, P. J. Kelly, and P. M. Fauchet, "Femtosecond Carrier-Carrier Interactions in GaAs," to be published in the *Proceedings of the Eighth International Conference on Ultrafast Phenomena*, Antibes-Juan-Les-Pins, France, 8–12 June 1992.

T. Gong, P. M. Fauchet, J. F. Young, and P. J. Kelly, "Subpicosecond Hot-Hole Dynamics in Highly Excited GaAs," to be published in *Applied Physics Letters.*

T. Gong, L. X. Zheng, K. B. Ucer, J. F. Young, P. J. Kelly, G. W. Wicks, and P. M. Fauchet, "The Role of Carrier-Carrier Interactions in Relaxation of Hot Carriers Excited at 2 eV in GaAs," to be published in *Physical Review B*.

T. Gong, L. X. Zheng, W. Xiong, W. Kula, R. Sobolewski, and P. M. Fauchet, "Femtosecond Optical Response of Y-Ba-Cu-O Thin Films: The Dependence on Optical Frequency, Excitation Intensity, and Electric Current," to be published in *Physical Review B*.

T. Gong, L. X. Zheng, W. Kula, W. Xiong, R. Sobolewski, and P. M. Fauchet, "Ultrafast Response of Current Carrying Y-Ba-Cu-O Thin-Film Strips," to be published in the *Proceedings of Ultrafast Electronics & Optoelectronics*, San Francisco, CA, 25–27 January 1993.

T. Gong, L. X. Zheng, W. Xiong, W. Kula, R. Sobolewski, P. M. Fauchet, J. P. Zheng, H. W. Kwok, and J. R. Gavaler, "Femtosecond Spectroscopy of Y-Ba-Cu-O Thin Films," to be published in the *Proceedings of the 6th Annual Conference on Superconductivity and Applications*, Buffalo, NY, 15–17 September 1992.

Conference Presentations

C. P. Verdon, "Hydrodynamics of Direct-Drive Inertial Confinement Fusion Capsule Implosions," AIAA 23rd Plasmadynamics & Lasers Conference, Nashville, TN, 6–8 July 1992.

The following presentations were made at the 22nd Annual Anomalous Absorption Conference, Lake Placid, NY, 12–17 July 1992:

R. E. Bahr, W. Seka, R. S. Craxton, and A. Simon, "Stimulated Raman Scattering in Long-Scale-Length Plasma Experiments on OMEGA."

H. Chen, J. A. Delettrez, B. Soom, S. Uchida, B. Yaakobi, and D. D. Meyerhofer, "K_α Emission from High-Contrast, Picosecond Laser-Plasma Interactions."

R. S. Craxton and F. S. Turner, "Refractive Image Distortion—An Alternative to Interferometry for Characterizing Long-Scale-Length Plasmas."

J. A. Delettrez, S. Gutstein, S. Uchida, and D. D. Meyerhofer, "Effect of the Ponderomotive Force on Fast Ions in Short-Scale-Length Laser-Plasma Interactions."

E. M. Epperlein, R. W. Short, and A. Simon, "Damping of Ion-Acoustic Waves in the Presence of Electron-Ion Collisions."

E. M. Epperlein, P. Amendt, L. Powers, and L. J. Suter, "Nonlocal Heat Transport in Spherical Plasmas Using the Fokker-Planck Code *SPARK*."

R. Epstein, B. Yaakobi, and F. J. Marshall, "The Role of Continuum Lowering in Opacity Calculations for Simulations of Diagnostic Spectra."

J. Li, C. J. McKinstrie, and A. L. Gaeta, "Nonlinear Oscillation and Chaos in Backward Four-Wave Mixing."

C. J. McKinstrie, X. D. Cao, and J. Li, "The Nonlinear Detuning of Multiwave Interactions."

D. D. Meyerhofer, A. C. Gaeris, and R. W. Short, "The Stimulated Brillouin Scattering Threshold in a Homogeneous CH Plasma."

W. Seka, R. E. Bahr, R. S. Craxton, R. W. Short, A. Simon, D. S. Montgomery, and A. Rubenchik, "Two-Plasmon-Decay Instability and Raman Scattering in Long-Scale-Length Laser Plasmas."

R. W. Short and E. M. Epperlein, "Thermal Stimulated Brillouin Scattering in Laser-Produced Plasmas."

A. Simon, E. M. Epperlein, and R. W. Short, "The Effect of Weak Electron-Ion Collisions on Ion-Sound Wave Damping."

S. Uchida, H. Chen, Y.-H. Chuang, J. A. Delettrez, and D. D. Meyerhofer, "Measurements of the P-Polarized Intensity Enhancement in High-Contrast, Picosecond Laser-Produced Plasmas."

J. J. Armstrong and T. J. Kessler, "Holographic Recording of Large-Aperture, High-Efficiency, High-Damage-Threshold, Transmission Diffraction Gratings," SPIE's 1992 International Symposium on Optical Applied Science and Engineering, San Diego, CA, 19–24 July 1992.

D. Gupta, W. R. Donaldson, and A. M. Kadin, "High-Temperature Superconducting Opening Switches," Fifth SDIO/ONR Pulse Power Meeting, 1992, College Park, MD, 17–19 August 1992.

R. L. McCrory, "Physics of Direct-Drive Inertial Confinement Fusion," International Conference on the Physics of Strongly Coupled Plasmas, Rochester, NY, 17–21 August 1992.

The following presentations were made at the 1992 Applied Superconductivity Conference, Chicago, IL, 23–28 August 1992:

D. Gupta, W. R. Donaldson, K. Kortkamp, and A. M. Kadin, "Optically Triggered Switching of Optically Thick YBCO Films."

W. Kula and R. Sobolewski, "Measurements of Low-Magnetic-Field Microwave Absorption in 110-K Superconducting Bi-Sr-Ca-Cu-O Thin Films."

R. Sobolewski, W. Xiong, and W. Kula, "Patterning of Thin-Film High-T_c Circuits by the Laser-Writing Method."

The following presentations were made at the 6th Annual Conference on Superconductivity and Applications, Buffalo, NY, 15–17 September 1992:

T. Gong, L. X. Zheng, W. Xiong, W. Kula, R. Sobolewski, P. M. Fauchet, J. P. Zheng, H. W. Kwok, and J. R. Gavaler, "Femtosecond Spectroscopy of Y-Ba-Cu-O Thin Films."

A. M. Kadin, D. Gupta, D. D. Mallory, M. Takahashi, W. R. Donaldson, and J. K. Truman, "Fabrication, Properties, and Applications of *In Situ* Sputtered YBCO Films."

W. Kula and R. Sobolewski, "Influence of the Crystalline Structure of Critical Current Density of Bi(Pb)-Sr-Ca-Cu-O Thin Films Superconducting above 100 K."

W. Xiong, W. Kula, R. Sobolewski, and J. R. Gavaler, "Superconducting Properties of Laser-Annealed Lines Fabricated in Oxygen-Deficient Y-Ba-Cu-O Thin Films."

The following presentations were made at the OSA Annual/ILS '92, Albuquerque, NM, 20–25 September 1992:

Y. Lin, T. J. Kessler, and G. N. Lawrence, "Calculations of Raman Conversions and Beam Quality of High-Intensity Laser Beams Propagated in Air."

D. D. Meyerhofer, S. Augst, B. Buerke, and J. Peatross, "Laser Ionization of Noble Gases with Linear and Circular Polarization."

The following presentations were made at the 20th International Congress on High Speed Photography and Phototonics, Victoria, BC, Canada, 21–25 September 1992:

P. M. Bell, J. D. Kilkenny, O. L. Landen, R. L. Hanks, J. D. Wiedwald, and D. K. Bradley, "The Gating of X-Ray Images in the 30–40-ps Region for Laser Plasma Experiments."

P. A. Jaanimagi and D. K. Bradley, "Neutron Streak and Framing Camera Diagnostics for ICF Implosions."

R. L. McCrory, J. M. Soures, C. P. Verdon, T. R. Boehly, D. K. Bradley, R. S. Craxton, J. A. Delettrez, R. Epstein, R. J. Hutchison, P. A. Jaanimagi, S. D. Jacobs, J. H. Kelly, R. L. Keck, T. J. Kessler, H. Kim, J. P. Knauer, R. L. Kremens, S. A. Kumpan, S. A. Letzring, F. J. Marshall, P. W. McKenty, S. F. B. Morse, W. Seka, R. W. Short, M. D. Skeldon, S. Skupsky, and B. Yaakobi, "Direct-Drive Laser Fusion Target Physics Experiments," 14th International Atomic Energy Agency (IAEA) International Conference on Plasma Physics and Controlled Nuclear Fusion Research, Wurzburg, Germany, 30 September–7 October 1992.

ACKNOWLEDGMENT

The work described in this volume includes current research at the Laboratory for Laser Energetics, which is supported by New York State Energy Research and Development Authority, the University of Rochester, the U.S. Department of Energy Office of Inertial Confinement Fusion under agreement No. DE-FC03-85DP40200, and other agencies.

UNIVERSITY OF
ROCHESTER